On the Nebular Motions of Sharpless 2-106 and its Evolutionary Phase

JOHN FAULHABER
Department of Astrophysical and Planetary Sciences
University of Colorado Boulder

Honors Thesis Committee

DR. JOHN BALLY, Thesis Advisor
Department of Astrophysical and Planetary Sciences

DR. ANN-MARIE MADIGAN, Honors Council Representative
Department of Astrophysical and Planetary Sciences

DR. HARRISON STALVEY, Thesis Committee Member
Department of Mathematics

Defense
4/7/2020

Abstract

Various details of the mechanisms and transitions that occur during massive star formation elude the scientific community due to inherent observational limitations. Sharpless 2-106 (S106) provides an opportunity to study the transitionary phases in massive star formation. S106 exhibits bipolar morphology, and has unprecedentedly fast nebular proper motions of up to ~120 kms^{-1}, many times the sound speed in photo-ionized plasma. Velocity analysis of the S106 nebula is presented to allow for classification of its evolutionary state. Data implies a transitionary state, and demonstrates nebular proper motions increasing with distance from the ionizing source. This points to three possible models: [1] The central star, S106 IR, may have experienced an explosion a few millennia ago that initiated the nebular motions. [2] The nebular motions may be associated with a dense expanding shell produced by stellar winds. [3] The evolving nebula consists of recently ionized ejecta, launched during a bipolar-molecular outflow phase during accretion.

Key words: Sharpless 2-106 (S106), Sound speed, Velocity, Morphology, Massive star, Proper motion, Evolutionary phase

Contents

List of Tables

[Quick reference]

List of Figures

[Quick reference]

Introduction

The various processes and mechanisms involved in the birth and evolution of massive stars ($M > 8\ M_\odot$, $10^3\ L_\odot < L < 10^6\ L_\odot$) remain as some of the least well understood aspects of star formation. Massive stars play a large role in the universe, and profoundly impact their immediate surroundings. Better understanding of these processes and mechanisms is critical if an accurate and comprehensive model of stellar formation is to be formed. Sharpless 2-106 (S106) provides a unique opportunity to study the transitionary stage from massive protostar to a mature main sequence star, surrounded by an HII region. Of particular interest is the timeline of events that take place during this transition. Recent examinations of S106 demonstrate an incredibly dynamic morphology, containing properties unique to very young stars, as well as those unique to stars further along in the developmental sequence. S106's morphology may shed some light on certain aspects of the timeline of high-mass star formation.

The purpose of this paper is to analyze the nebular motions of S106's primary lobe structures and propose a classification of the current evolutionary stage of S106, as well as a model for the cause of its morphology. Section 1 will discuss the details of S106. Section 2 will introduce the data. In section 3, an analysis of the velocities of S106's nebular motions is presented. Section 4 will then provide overviews of relevant processes and environments to aid interpretation of the data and analysis. In section 5, interpretation of the data and analysis is presented. Section 6 will then summarize the findings and briefly examine future prospects, concluding the paper.

A Note on Scope

As will be explored in later sections, the S106 system is equally peculiar as it is dynamic. A comprehensive analysis of the S106 system would be a very large project, and lies outside the scope and purpose of this paper. Instead, the results of the analysis presented here will allow for more detailed structural models of the S106 nebular region to be created, which in turn will allow for more exhaustive analyses to be performed in future studies. Accordingly, an additional paper, to be published, is concurrently being written which explores in greater detail the environment of S106, and further implications of the potential causes for S106's particular morphology, using some of the results presented here. As stated in the introduction, only motions of the S106 nebular structure will be directly analyzed in this paper, namely those of its immediate lobes.

Part I

The System, Data, and Analysis

Section 1 - Sharpless 2-106

Sharpless 2-106 is an extremely prominent bipolar nebula/HII region located in the constellation Cygnus at galactic coordinates l=76.4º b=-0.6º, and likely formed in the highly prolific stellar nursery of Cygnus X. The central star of S106, S106 IR, is a pre-main-sequence (PMS) 5-day-period binary system with a luminosity of ~20,000 $L_\odot$, emitting copious amounts of radiation. S106 IR consists of a ~20 $M_\odot$ O9 primary star, and 3 $M_\odot$ secondary star, with a separation ≲ 0.2AU (Comerón et al. 2018). Recent parallax measurements at radio wavelengths towards the 22 GHz H_2O maser from the Class 0 source S106 FIR (Furuya et al. 1999), a local star to S106 IR, give a distance of 1.3 kpc (Xu et al. 2013), though only utilize the single S106 FIR star. The most reliable distance estimates for S106 use Gaia DR2 distances towards dozens of stars in the S106 molecular cloud that lie both in front of, and behind, the cloud. The parallax at which extinction and reddening abruptly increase within the cloud yield a distance of 1,091±54 pc (Zucker et al. 2019). A distance of 1,091 pc is used for the presented analysis in this paper. The ionized gas immediately surrounding S106 IR consists of two lobes, constricted around the middle by a molecular disk, and S106 IR itself is heavily obscured in optical wavelengths. Bally et al. (1983) found S106 IR has a mass loss rate of ~10^{-6} $M_\odot$ yr^{-1}. Additionally, studies done by Anker et al. (2000) revealed S106 is dominated by a photo-disassociation region (PDR), as opposed to shock emission. This is to say S106 is flooded with ultraviolet photons which perform a vast majority of the molecular interactions within the

nebula, and produce much of the ambient radiative energy. Molecular hydrogen lines in S106 IR's spectrum are consistent with PDR excitation conditions (Fig. C) (Hodapp & Schneider 2008). The northern lobe of the S106 nebula is pointing away from the observer, and is redshifted by ~30 kms^{-1}, while the southern lobe is blueshifted by a similar value (both with respect to the host cloud) (Hodapp & Schneider 2008). The nebula's bifurcating disk was observed by Gibb & Hoare (2007) and Hoare & Muxlow (1996)[1] using cm-interferometry, and consists of cold gas, while it is very prominent in optical wavelengths. A secondary feature of the bifurcating molecular disk is a dark lane of matter that appears to be interacting with the disk. The exact nature of the dark lane is debated. Figure D is a 3D model depicting the disk and dark lane.

Fig. A: Sharpless 2-106

(Oasa et al. 2006)

Near-infrared J, H, and K band composite image of Sharpless 2-106, taken by the Cooled Infrared Spectrograph and Camera (CISCO) instrument on the Subaru telescope. Most of the main components of Sharpless 2-106's structure can be seen in this image.
The poorly columnated bipolar outflows are particularly distinct (blue).

[1] Schneider et al. 2018

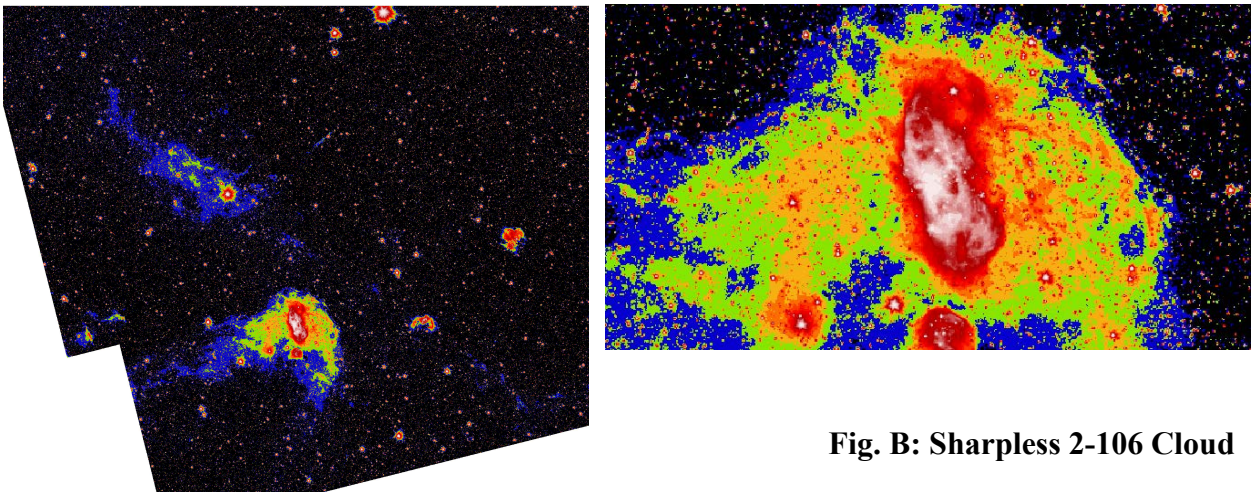

Fig. B: Sharpless 2-106 Cloud

Left: Zoomed out view of Sharpless 2-106 and its surrounding cloud.
Right: Closer-in image of Sharpless 2-106, in white.
In these images, Sharpless 2-106 is tilted at roughly the same angle as in figure A.

There is some debate over whether or not the disk feature of S106 is an accretion flow or an evaporating filamentary structure/material dispersal flow. From velocity flow measurements alone, it is difficult to discriminate between the two theories. In fact, the former was proposed by Bally et al. (1983), while the latter was proposed by Hodapp & Rayner (1991), and both theories were proposed together by Balsara et al. (2001)[2]. Studies on S106's magnetic field by Vallée & Fiege (2005) show B-field lines that run parallel to the dark lane, and such is consistent with the accretion theory (Schneider et al. 2018). Additionally, simulations done by Peters et al. (2010) of models of massive rotating cloud core collapse are also consistent with the accretion model for S106 (Schneider et al. 2018). Though it is not currently possible to definitively determine if accretion is still occurring in S106, some information can be inferred. Research published by Hosokawa & Omukai (2009) demonstrates accretion rates in excess of 10^{-5} $M_{\odot}$ will cause a PMS star to swell up to AU scale radii. Since it is evident S106 IR is not bloated, we can know S106 is

[2] Schneider et al. 2018

at minimum not accreting at accelerated rates (though future research may reveal forming stars cycle through bloatations, in which case the former point is rendered moot).

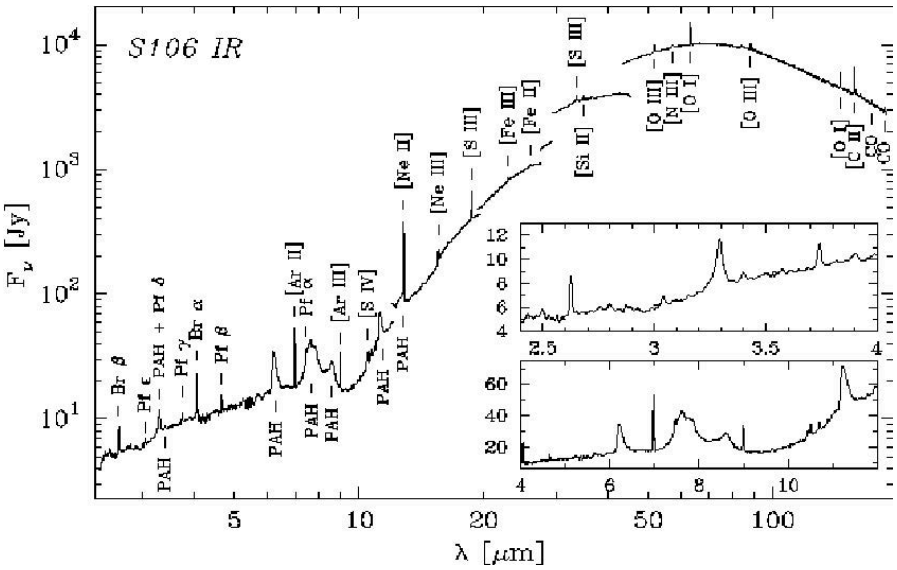

Fig. C: Sharpless 2-106 Spectrograph

(Ancker et al. 2000)

ISO SWS and LWS spectrum of S106 IR.

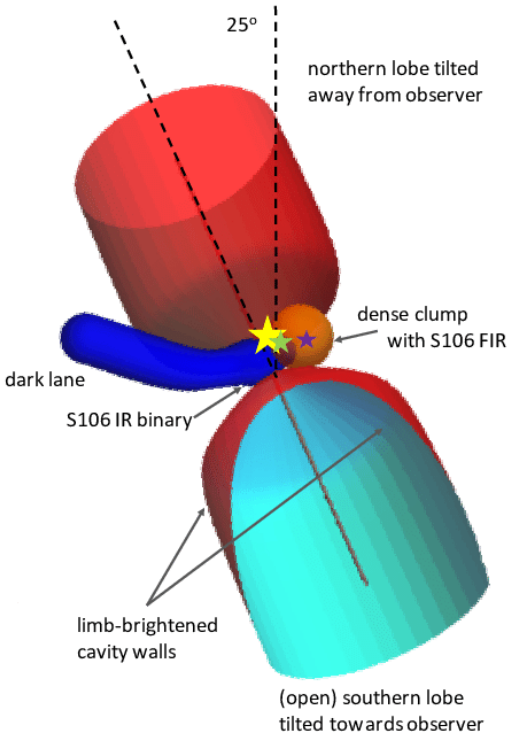

Fig. D: 3D Sharpless 2-106 Model

(Schneider et al. 2008)

3D model of Sharpless 2-106. The dark lane can be seen here in blue. Whether the dark lane is feeding or carrying material away from the circumstellar disk is debated.

The bipolar lobes of S106 exhibit incredible nebular proper motions of over 100 kms^{-1}, many times greater than the usual and expected value for such regions. Figures E-H below show motions of the bipolar lobes over 15.2 years.

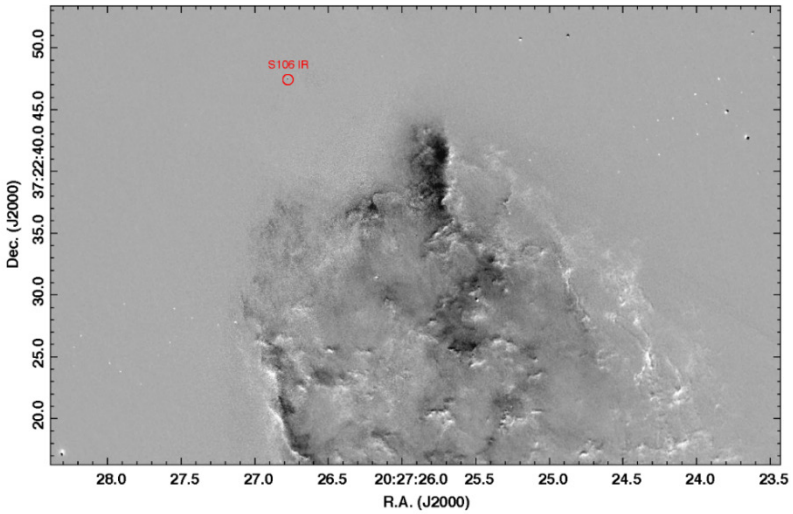

Fig. E: 15 Year Motions (South Lobe A)

Difference image of 1995 and 2011 HST data. The shadows demonstrate proper motions. The constituent images have a time interval of 15.2 years. This is the southern lobe of Sharpless 2-106.

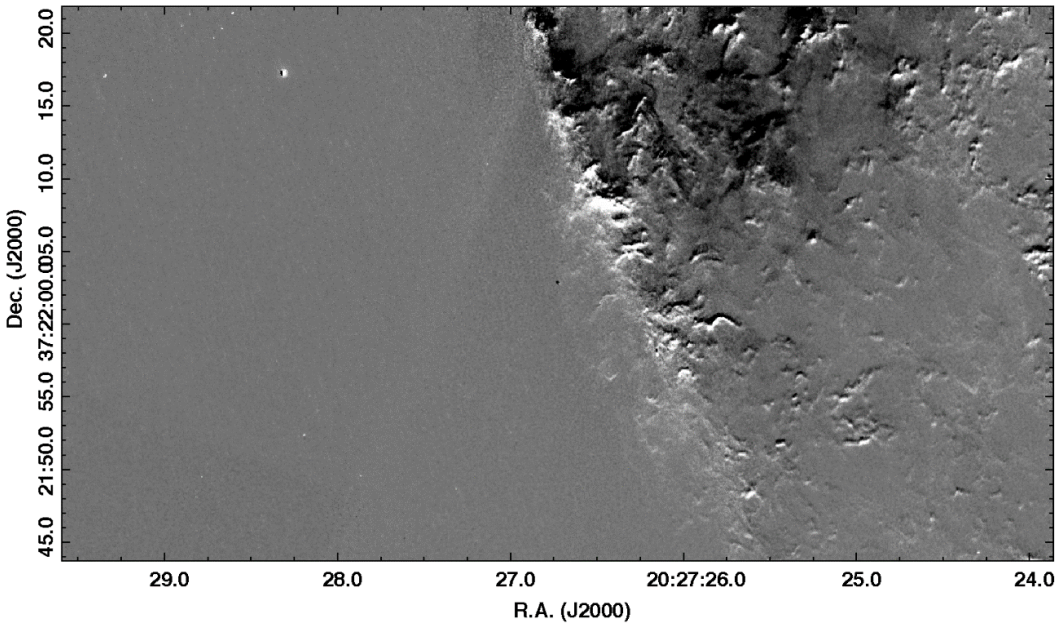

Fig. F: 15 Year Motions (South Lobe B)

Difference image of 1995 and 2011 HST data. The shadows demonstrate proper motions. The constituent images have a time interval of 15.2 years. This is a closer view of the lower left region of the southern lobe of Sharpless 2-106.

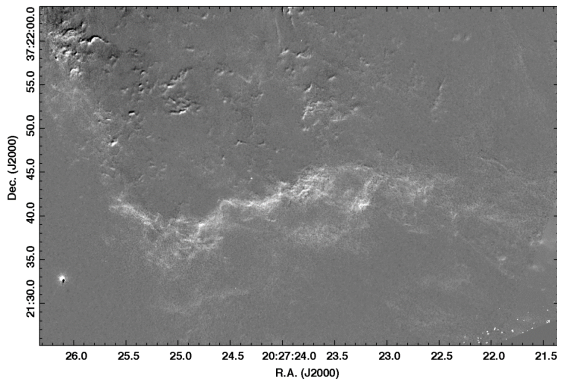

Fig. G: 15 Year Motions (South Bar)

Difference image of 1995 and 2011 HST data. The shadows demonstrate proper motions. The constituent images have a time interval of 15.2 years. This is the southern bar of Sharpless 2-106.

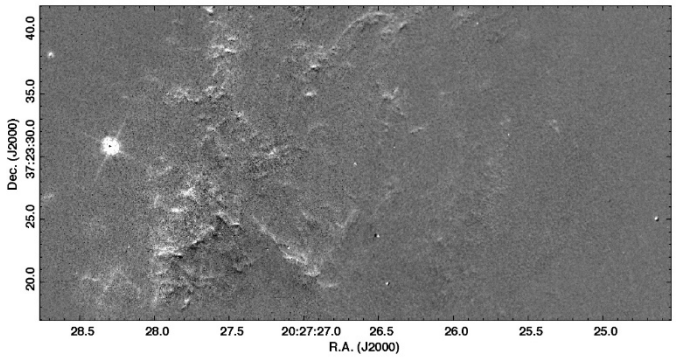

Fig. H: 15 Year Motions (Inner Region)

Difference image of 1995 and 2011 HST data. The shadows demonstrate proper motions. The constituent images have a time interval of 15.2 years. This is a closer view of the inner region of Sharpless 2-106.

For a detailed review on the history of study on the S106 system, Hodapp & Schneider (2008) is recommended.

Section 2 – Data

The specific analysis performed for this study determines the true velocities of gas within the bipolar outflows of S106, and requires proper motion data and radial velocity data. Proper motions were calculated from HST images of S106. Radial velocity data was taken from Solf & Carsenty (1982).

The main two HST images used were taken during observing runs of S106 by HST in 1995 under GO program 5963 (Bally et al. 1998) targeting Hα with WFPC2, and in 2011 using WFC3 (GO program 12326: PI Keith Noll) targeting [N_{II}] 6584Å, HeII 4686Å, [O_{III}] 5007Å and the 1.1 and 1.6 μm continuum using the wide-band filters F110W and F160W. Registration of

the 1995 and 2011 images using field stars reveals that many field stars have proper motions many times larger than the point-spread-function. Thus, the positions and proper motions of field stars from Gaia DR2 (Gaia Collaboration et al. 2016, 2018) were used to improve both the distortion corrections and astrometric registration of the 1995 and 2011 images. The Gaia DR2 positions are referenced to epoch 2015.5. The Gaia DR2 proper motions (and proper motion errors) were used to estimate the positions of about 70 stars in the field of view of the S106 HST images at the time the 1995 and 2011 images were obtained. The pixel coordinates of these stars in each HST images were matched to the R.A. and DEC. positions estimated by back-tracing the Gaia DR2 proper motions. IRAF routines CCMAP and CCSETWCS were used to determine the mapping of the pixel coordinates to the celestial coordinates. For the southern lobe of S106, stellar positions for the 1995 image were back-traced by 20.0 years (7289 days), corresponding to the interval between the Gaia DR2 reference epoch and the observation date of the 1995 images; the northern lobe positions were back-traced by 19.5 years (7123 days). For the 2011 image, stellar positions were back-traced by 4.4 years (1599 days). Inspection of 57 stellar objects, shown in figure I, for which Gaia DR2 proper motions were obtained on the registered images shows that registration has a 1σ error of about 2 to 3 mas yr^{-1}. Unfortunately, the southern part of S106 where the bright-bar is located in figure I (close-up in Fig. G) has few stars. The registration in this part of the image may have at least a factor-of-two larger error because this portion of the image is close to the edge of the field imaged in 1995 and 2011. Table 1 lists observation metadata for the images.

Fig. I: Gaia DR2 Stars

An HST WFC3 image showing Sharpless 2-106 in the narrow-band [Nii] filter F658N that excludes the H emission line. This image was obtained in 2011. The cyan circles mark the locations of stars for which Gaia DR2 provides proper motions. The image is rotated so North is vertical.

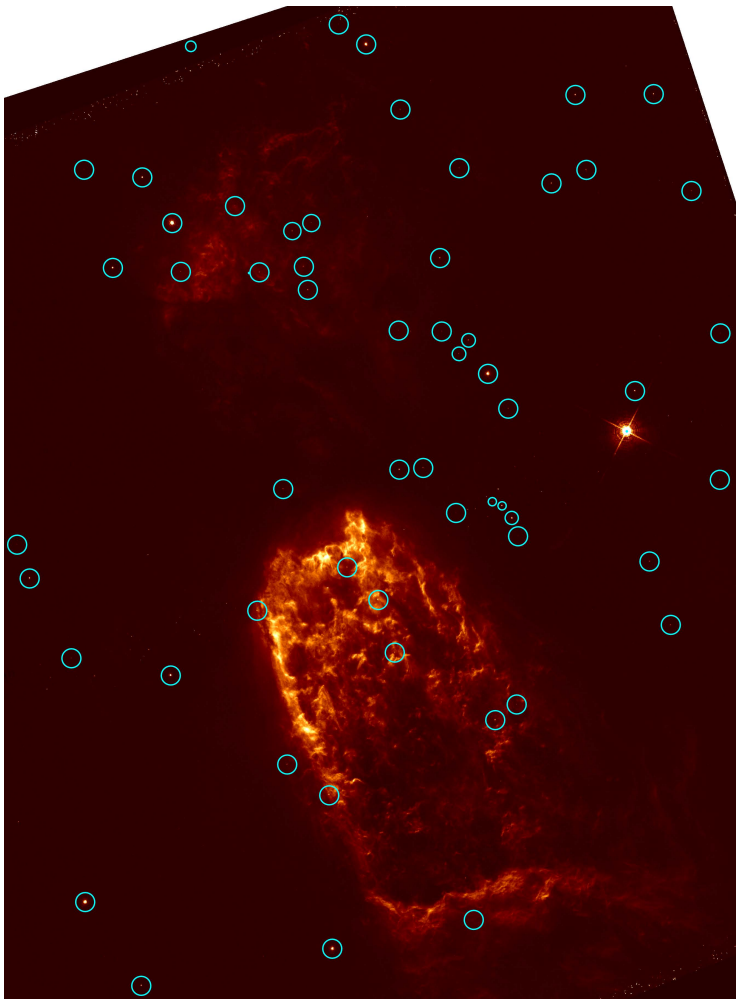

Table 1. Observation Metadata

Field	Date	MJD	Inst.	Filter	Exp.
S106N2	30 Dec 1995	50081	WFC2	F656N Hα	1200s
S106N	30 Dec 1995	50081	WFC2	F656N Hα	1600s
S106S	17 Jul 1995	49915	WFC2	F656N Hα	1600s
S106	12 Feb 2011	55604	WFC3	F658N [N_{II}]	2400s
S106	13 Feb 2011	55605	WFC3	F110W	1198s
S106	13 Feb 2011	55605	WFC3	F160W	1198s

The radial velocity data used, presented by Solf & Carsenty (1982), was taken with observations of the S106 nebula using the large coudé spectrograph of the 2.2-m telescope on Calar Alto, Spain. Using the f/3 camera and 1.1" x 117" slits projected onto the sky under excellent seeing conditions, 27 spectra and radial velocity fields were secured. The observed second order spectral range between 6470 and 6770 Å includes the lines of Hα, HeI λ6678, [N_{II}] λλ6548, 6583 and [S_{II}] λλ6717, 6731. The obtained spectral resolution is about 12 kms^{-1}. The spectrum plates were calibrated using a device on the same spectrograph and a single Lyot-filter element, according to methods described by Trefzger & Solf (1978). Additionally, long slit comparison spectra were recorded separately, in order to determine any geometrical distortion introduced by the image tube. With all corrections applied, radial velocity variations along the slits could be determined within ± 0.5 kms^{-1} rms at intervals corresponding to 2" on the sky. A possible systematic error among velocities derived from the same line, due to relatively coarse spacing between the comparison lines, may be up to ± 2 kms^{-1}. Photometric calibration was estimated to be accurate within 15%, with larger error for larger densities.

The specific primary regions within S106 chosen for velocity analysis are marked by blue x's, and numbered, in figures J and K on the following page.

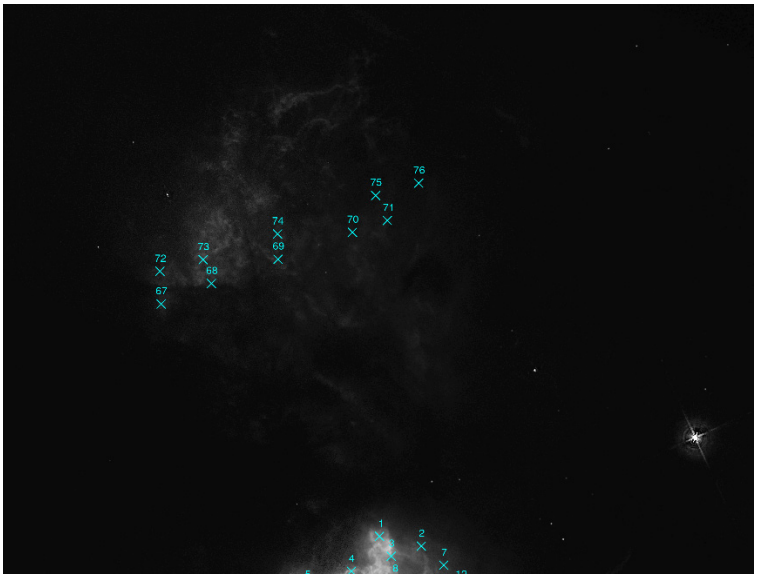

Fig. J: Sharpless 2-106 Northern Regions (Primary)

Here can be seen the selected primary regions, or “clumps,” used for analysis of the northern lobe of Sharpless 2-106.

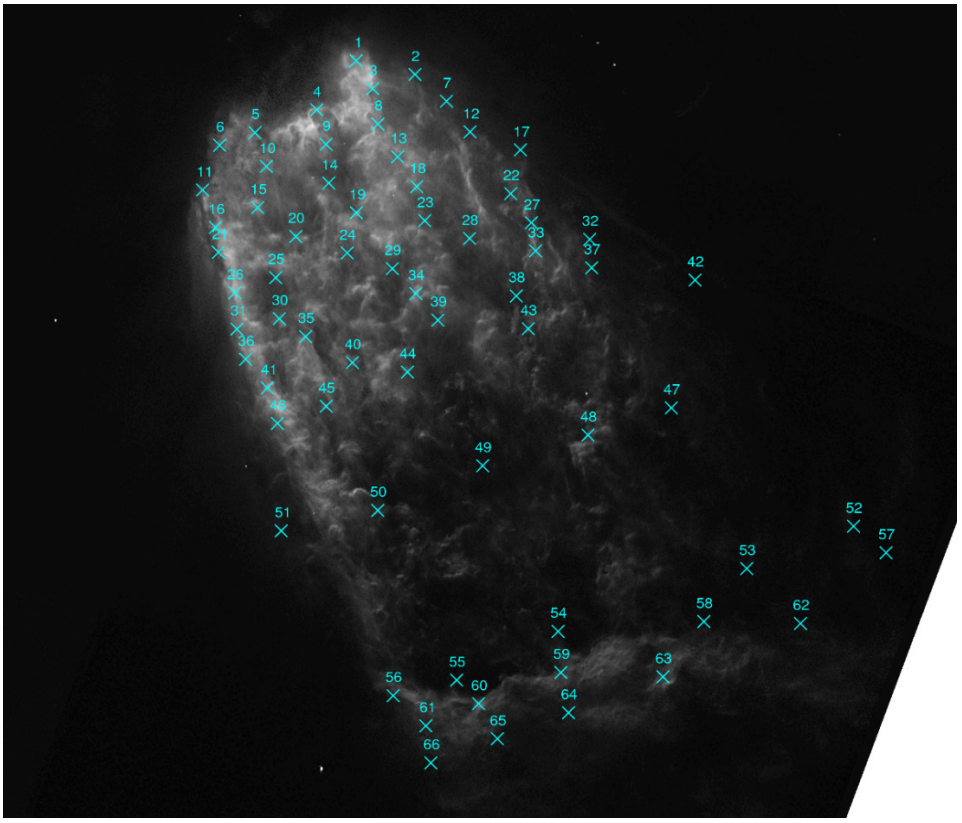

Fig. K: Sharpless 2-106 Southern Regions (Primary)

Here can be seen the selected primary regions, or “clumps,” used for analysis of the southern regions of Sharpless 2-106.

Section 3 – Velocity Analysis

The following sections will discuss in detail the various methods used during analysis, as well as present the results.

Section 3.1 - Proper motions

To determine the proper motions of the specified regions within the bipolar lobes, code was written that utilizes SAOImageDS9 region files with pre-selected regions, along with calculations, to directly extract the proper motion of every specified region. Upon feeding the code a region file for both the 1995 and 2011 images, with corresponding specified regions, the sexagesimal coordinates for each region specified are extracted. The sexagesimal coordinates are then combed for the R.A. and DEC. values, which are pulled out and converted to degrees by dividing the minute values by 60 and second values by 3600. Once this is complete, the resulting values are compiled into lists – one for the 1995 data, and one for 2011 data. Following this, the lists are used to calculate angular separation distances between corresponding regions (1995-2011). Because the observed proper motions over the ~15 year interval are on the order of 100's of milli-arcseconds, a very specific method was introduced to calculate the distances.

One method to calculate angular distances is to construct vectors

$$\hat{n}_i = \begin{bmatrix} \cos\delta_i \cos\alpha_i \\ \cos\delta_i \sin\alpha_i \\ \sin\delta_i \end{bmatrix}, \text{ where } \delta \text{ is declination and } \alpha \text{ is right ascension,}$$

and utilize the dot product $\hat{n}_1 \bullet \hat{n}_2 = \cos\theta_{12}$ to perform

$$\cos(\theta_{12}) = \sin(\delta_1)\sin(\delta_2) + \cos(\delta_1)\cos(\delta_2)\cos(\alpha_1 - \alpha_2).$$

This method has limitations, however, and loses much accuracy when dealing with small angles, such as fractions of an arcminute. Instead, the Haversine formula (below) yields much better results:

$$\theta_{12} = 2\arcsin\left(\sqrt{\sin^2\left(\frac{\delta_2-\delta_1}{2}\right) + \cos\delta_1\cos\delta_2\sin^2\left(\frac{\alpha_2-\alpha_1}{2}\right)}\right).$$

Although the Haversine formula is slightly anachronistic, there is much literature on its advantages, such as R.W. Sinnott's recollection of the formula in the December 1984 issue of *Sky and Telescope*, where he discusses its advantages over the simple law of cosines in calculating angular distances between objects in the sky with very small angular separations. Accordingly, the Haversine formula was used for the presented analysis in this paper[3].

The lists of degree R.A. and DEC. values are fed into the Haversine formula, and the resulting angular distances, in radians, are multiplied by 206265 to get back units of arcsecond.

The following equation is then used to calculate the corresponding tangential velocities of the observed proper motions:

$$V_T[kms^{-1}] = 4.74\left(\frac{angular\ distance}{15}\right)[\text{arcsec}\,yr^{-1}]d[pc],$$

Where the factor of $\frac{1}{15}$ accommodates for the ~15 year interval between the 1995 and 2011 images, and a value of 1,091 pc for *d*, the distance to S106, was used, as mentioned in section 1.

[3] Within geodesy Vincenty's formulae are the most accurate for determining these sorts of distances, however, the algorithm is very hairy, and overkill for the analysis performed. Thus, the Haversine formula was sufficient.

Section 3.2 – Radial and True Velocities

Once the tangential velocities were found, they were then used in conjunction with corresponding radial velocities from Solf & Carsenty (1982) (S&R) to determine an estimate for the true velocity of each region chosen. Although the calculation itself only uses the Pythagorean theorem, determining numerical values from the S&R data required some work. When choosing the primary regions for analysis, gaseous clumps that lined up as closely as possible to the slit positions j-zz of Fig. 1 from S&R, reproduced here as figure L in Appendix B, were chosen by overlaying the 1995 HST image with the S&R Fig. 1. This was to allow for the use of the data plotted in S&R Fig. 5j-zz, reproduced here as figure M in Appendix B, during analysis. In order to determine numerical values for the data, the plots for slits j-zz were blown up on separate sheets of paper and individually manually split horizontally into 32^{nds} and vertically into 18^{ths}, individually to accommodate for any inconsistencies in the original printing of the plots, given the nature of printing technology at the time of their production. Additionally, S&R Fig. 5j-zz itself was printed at a very slight angle. This was measured and accounted for when drawing up the subdivisions for each plot.

To determine which points of data in the S&R plots corresponded to the chosen regions in the HST data, the 1995 HST image and S&R Fig. 1 were printed out and a scaling factor between the two printed images was determined for each long-slit measurement. Using this and manual measurements from the middle of each long-slit, so as to correspond to the middle of each radial velocity plot, corresponding positions on the divisions made on the S&R velocity plots were calculated, and radial velocity measurements within one 32^{nd} division were selected. When determining the scaling factors, the scaling calculation was based on the percentage difference in sizing in the S&R Fig. 1 “grid boxes”, resultants from the crossing of the horizontal

and vertical long-slits, and the corresponding boxes on the printed HST image, resultants from when the two images were initially overlaid to aid in selection of the appropriate regions, and surrogate slits were drawn. Because the S&R long-slits are not all the same "length" and not all aligned, the conversion factors from measurements from the middles of the surrogate slits on the HST image to the S&R Fig 1 slits. and then to the corresponding amount of 32^{nds} over from the middle of each radial velocity plot had to be individually accordingly scaled and/or shifted. Any regions whose corresponding location on the radial velocity plots did not lie within one 32^{nd} of a data point were not included in the true velocity calculations. Lastly, three separate images were used for the HST image proper during scale calculation – one for the northern lobe of S106, one for the southern lobe, and one for the southern bar (figures P, Q, R, respectively, Appendix B). This was to allow for more resolvable graphics to aid in the manual measurements. All the images used and corresponding measurement extrapolations may be found in Appendix B and in Table 5. Please note tables 2 and 3 in Appendix A, discussed in the following section, contain the analysis results in a more readable fashion. Table 5 in Appendix B is given only to include all the values that were used. The results in tables 2 and 3 should be consulted first.

Section 3.3 – Velocity Analysis Results

The resulting velocity values for the chosen regions are presented in Table 2, in Appendix A. Figure O in Appendix B is a reproduction of the Solf & Carsenty Fig. 5j-zz with the chosen data points circled, while Table 4 (Appendix B) assigns numbers (corresponding to the related regions) to the circles. Values found for the true velocities were determined to have an error of roughly ± 3 kms^{-1}. However, due to the fact that the coordinates used for each gaseous

clump were determined by hand, human bias leading to random error across the proper motion values of up to 15% variance may be present.

In addition to the 76 regions chosen for true velocity calculation (the primary analysis), an additional 30 were chosen for their distinctive visual representation in the 1995 and 2011 HST images, and used exclusively for tangential velocity calculations. These are presented in Table 3, in Appendix A. Please note the numbers in Table 3 *do not* correlate to the same regions as listed in Table 2 and figures J and K. The additional 30 regions can be seen in figure S, below.

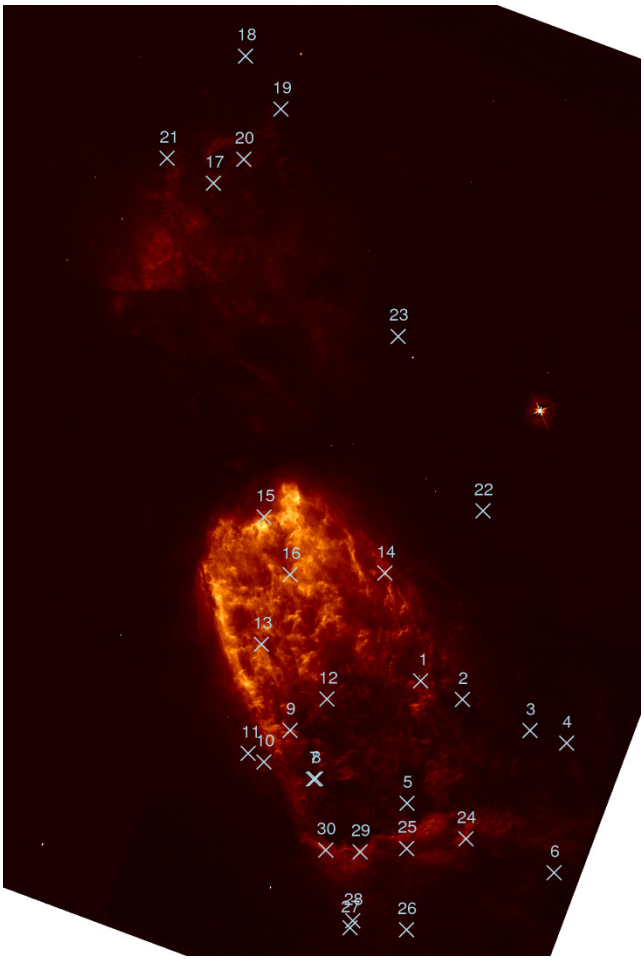

Fig. S: Sharpless 2-106 Regions (Secondary)

Here can be seen the selected secondary regions, or "clumps," used for analysis of Sharpless 2-106.

Projections of motion over 400 years for both the primary (Figs. J,K) and secondary (Fig. S) regions chosen were calculated as additional aids in analysis. For images with superimposed vector projections of motion over 400 years for each region, see figures T-Y in Appendix A.

Part II

Overviews and Interpretation

Section 4 – Overview of Relevant Processes and Environments

The following sections will provide a brief overview of the most important steps of low and high-mass star formation, as well as an overview of the basic stages and characteristics of star forming regions. If the reader is familiar with the relevant topics, they may skip to section 5, where comments on S106/S106 IR's evolutionary phase and which of three models best fits the system will be made.

Section 4.1 - Low-Mass Star Formation

Low-mass star formation begins with a cold, isothermal molecular cloud. Turbulence causes localized gravitational collapse from density structures into clumps, which leads to fragmentation into protostellar cores. As molecular infall builds the mass of the core, a distinct spherical structure emerges and becomes sufficiently large to accrete as a well-defined body, or protostar. The geometry of the accretion process morphs from isotropic infall into that of a disk due to conservation of angular momentum and a non-zero mean velocity of the cloud. By this phase, the protostar is still deeply imbedded in gas, and is generally only visible in far infrared and lower frequencies because the parent cloud is opaque in the near-infrared and visible bands of the spectrum, with the protostar not yet putting out high enough energy radiation to "shine through" (the region is "warm," and not "hot"). As the density of the protostar increases, it eventually becomes optically thick to its own radiation. Once this occurs, energy is prevented

from escaping the protostar, and temperatures are raised enough to initiate deuterium fusion (Fig. Z).

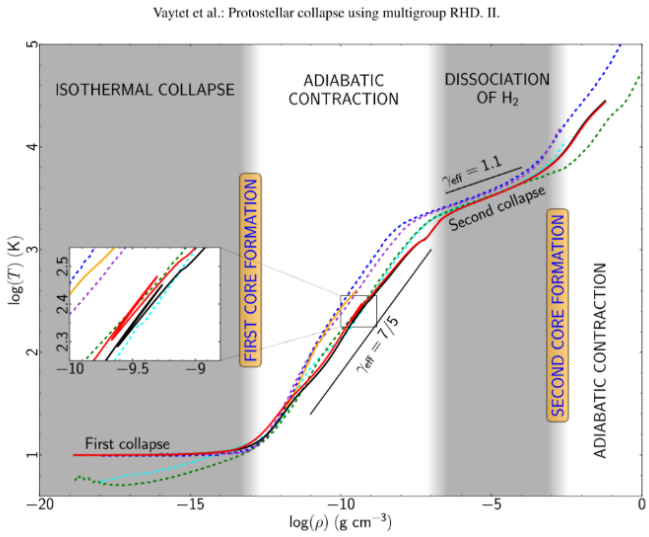

Fig. Z: Protostellar Core Evolution

(Vaytet et al. 2018)

Plot of density vs. temperature illustrating stellar core evolution from cloud collapse until formation of the "second" (proper) core. A drastic increase in temperature can be seen to occur during adiabatic contraction. Different colored lines show results from different models.

Radiation pressure from the fusion is high enough to blast through any remaining envelope of matter, and the result is a stable young stellar object (YSO), characterized by a circumstellar disk and well collimated bipolar outflows, or jets. This stage is adiabatic in nature. The jets carry away excess angular momentum with them, and are one of the primary mechanisms that allow YSOs to continue accreting mass (Max Planck Gesellschaft 2020). By the time hydrogen fusion initiates, most of the free material has accreted; the mass of any remaining envelope and disk material is no more than 10-20% that of the mass of the protostar (Motte et al. 1998). The YSO may now be considered a T Tauri star. T Tauri stars are visible in optical wavelengths, and otherwise have a standard PMS blackbody curve.

Fig. AA: 2D Protostar Model

(Greene 2001)

Here can be seen a structural model of a protostar. The bipolar outflow is clearly well-columnated.

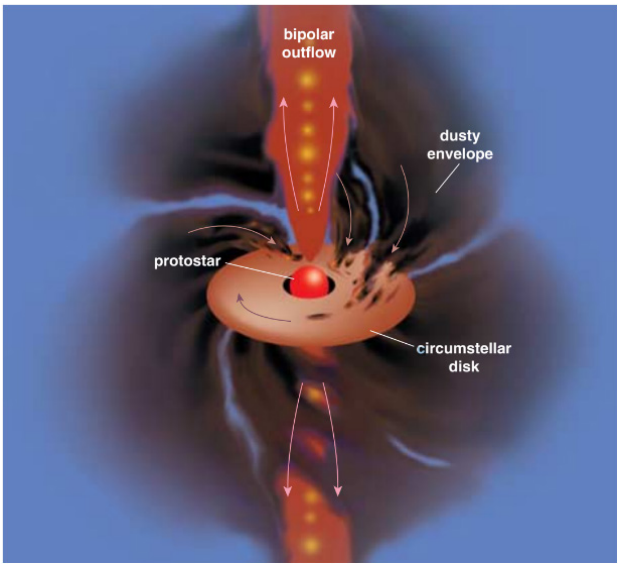

The general timeline after initial cloud collapse can be described through a series of class designations, suggested by Lada (1987):

Class 0 Source

Class 0 YSOs are hydrostatic, and are characterized by a well collimated outflow and dust envelope visible in sub-millimeter wavelengths. The stellar system HH 212 is an excellent example of a class 0 source, and can be seen in figure AB, in Appendix A.

Class I source

Class I YSOs are in a late stage of active accretion, and are characterized by much less collimated, less powerful outflows than class 0 YSOs. The Butterfly Star (IRAS 04302+2247) is a class I YSO, and can be seen in figure AC, in Appendix A. Around/during the period of class I classification, YSOs become optically visible.

Class II source

Class II YSOs have accumulated most of their mass, and have entirely dissipated their circumstellar envelopes. They have distinct circumstellar disks.

Class III source

Class III sources have lost most of, if not all of, their disks, and closely resemble main sequence stars.

Section 4.2 – High-Mass Star Formation and HII Region Evolution

High-mass star formation is more complicated than low-mass star formation. Despite the major role massive stars play in our universe, there are many gaps in our knowledge on their formative processes. In the words of Hans Zinnecker and Harold W. Yorke,

"*High dust extinction makes it difficult to observe high-mass stars during critical early formation phases. They are rare. They evolve quickly, and important evolutionary phases are short-lived. The theoretical problem is extremely complex. Finally, massive stars are seldomly (if at all) formed in isolation; the proximity of other high-mass stars compounds the complex influence of the forming star on its local environment via gravitational interactions, powerful outflows and winds, ionizing radiation, and supernovae.*" (Zinnecker & Yorke 2007).

As such, the following is, in general, topical basics of what we know about high-mass star formation, as are relevant to this paper.

Like low-mass star formation, high-mass star formation begins with molecular cloud collapse and fragmentation. The initial cause of contraction is not necessarily the exact same

between low-mass and high-mass stars, but regardless of the cause, the result is the formation of a protostellar core.

For more massive stars, further growth due to accretion alone is not yet guaranteed as a valid mechanism for evolution, as radiative pressure would halt accretion before the creation of a massive star. Duly, the pure accretion assumption was questioned by Bonnell et al. (1998) and Stahler et al. (2000)[4] who instead suggested that coalescence of less massive protostars may be the formation mechanism. On the other hand, the existence of commonly observed bipolar outflows from massive protostars suggests heavy accretion likely takes place in one form or another. Some combination of the two theories is likely the actual case. The presence of substantial accretion is assumed for this paper.

Early accretion during high-mass star formation occurs so quickly, there is effectively no pre-main sequence phase, and hydrogen burning begins almost immediately (Schneider et al. 2018). Given the denseness of the rapidly accreting material, massive YSOs (MYSOs) are highly obscured, and detection of the actual stellar object is generally only possible at wavelengths higher than mid-IR (Keto 2020) – the high column density of the immediate molecular cloud absorbs the optical and near-IR light (Hoare et al. 2006).

As accretion takes place, most stars will produce molecular bipolar outflows. Due to the imbedded nature of forming stars, these outflows inject energy and momentum into the surrounding gas. The energy and momentum injection rates increase with luminosity and mass (Maud et al. 2015), and so forming massive stars generally drive the most powerful molecular outflows in their natal cloud.

[4] Churchwell 2002

As growth continues, more radiation from the MYSO slams into the surrounding molecular cloud, and a hyper-compact HII (HCHII) region is formed. At some further radius from the MYSO, the HCHII region becomes an ultra-compact HII (UCHII) region. The leading edge of these compact HII regions expands outward at the sound speed

$$v_{sound\ in\ gas} = \sqrt{\frac{\gamma kT}{\mu m_H}},$$

where γ is the adiabatic constant, and slows as the density and pressure drop (Fig. AD). Prior to ionization, local sound speeds are generally ~.2 kms^{-1}. Expansion of ionization bubbles is expected to be at most ~10-11 kms^{-1}.

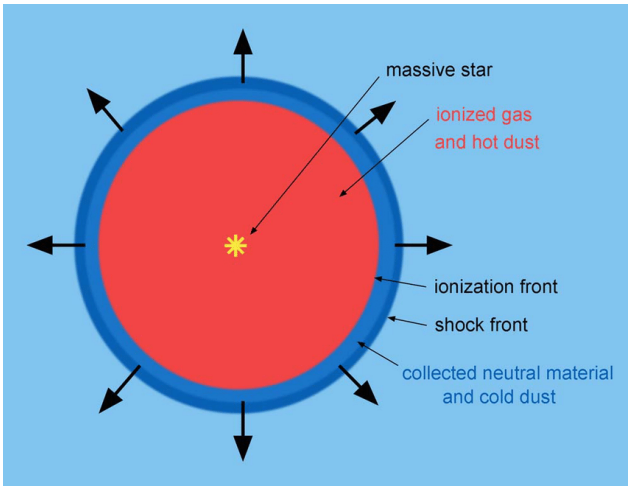

Fig. AD: HII Region Expansion

(Deharveng et al. 2010)

Here can be seen a depiction of an expanding ionization front. In general, such fronts expand isotopically. As R increases, density falls with $\sim \frac{1}{R^3}$.

The nature of HCHII regions is not yet well understood, as they are optically thick down to millimeter wavelengths, and all known instances of HCHII regions are associated with MYSOs, and imbedded along with their stars (Churchwell 2002). Neither HCHII nor UCHII regions exist in low-mass star formation. Dust surrounding UCHII regions is illuminated by the inner ionized regions out to very large radii, which allows for studying the surrounding density distributions and birth environments of massive stars (Hoare et al. 2006). This makes imbedded

HII regions an excellent indicator of high-mass star formation; the two are largely associated (Churchwell 2006; Anderson et al. 2009; Hoare et al. 2006).

Once MYSOs surpass ~15-20 $M_{\odot}$ and accretion subsides, they will begin to emit hydrogen-ionizing Lyman continuum radiation (Hosokawa et al. 2009). This radiation photo-ionizes the walls and interior of the remaining bipolar molecular outflow from the main accretion phase, and dissociates, heats, and further ionizes the parent cloud. Such feedback may halt stellar formation by blowing away the gas fueling growth.

Further distinctive traits of high mass star formation include the production of masers. In general, masers can be generated through a handful of different mechanisms (most often methanol masers trace disks, and water masers trace shocks inside outflows), but it is not uncommon to detect multiple from the same source. In particular, methanol and H_2O masers are particularly representative of high mass star formation, as they require incredibly high-energy environments – such as an UCHII region – to form. The nature and qualities of stellar masers can be used to pinpoint a more exact evolutionary placement of their source MYSO/system within the maser phase; molecular makeup of the masers may yield information on the structure of the molecular cloud (information indicative of a specific stage). Breen & Ellingsen (2012) is recommended for further details regarding this form of analysis.

Extremely violent, poorly columnated bipolar outflows near the poles of the forming star are also characteristic of MYSOs. Similar to the bipolar outflows of class I YSOs (except on a much larger scale), the outflows allow incredible amounts of radiation to escape without impeding accretion. These outflows form early on, around the time accretion becomes non-isotropic.

Timescales of MYSO evolution follow the Kelvin-Helholtz time scale:

$$t_{KH} = \frac{GM^2}{RL},$$

Where G is the gravitational constant, M is the mass, R is the radius, and L is the luminosity. As a result, MYSOs reach the main sequence extremely fast due to their high luminosities (typically $10^3\ L_\odot < L < 10^6\ L_\odot$).

The Lada classifications also apply to massive stars, though distinctions become less coherent. Masers, for instance, are often observed as emitted from class 0 YSOs.

Zinnecker & Yorke (2007) is recommended for a more in-depth review of the formation processes of massive stars, as well as a general look at the competing theories.

Section 4.3 – Natal Clouds

In general, there are two distinct characteristic regions found during stellar evolution. Stellar nurseries, and mature HII regions. They represent opposite ends of the formative timeline, and any systems in an in-between stage will generally share properties of both.

Stellar nurseries are simply active star forming regions. The Kleinmann–Low nebula in Orion (Fig. AE, Appendix A), or Orion-KL, is one of the most active nearby massive star forming regions. Morphologically, it shows all the characteristics of such a region – water masers, HII regions, etc. It is also a representative example of a stellar nursery, and so its features will be used for reference.

Namely, within Orion-KL is a star referred to simply as Orion Source 1. Orion Source 1 is a characteristic forming massive star, though, unlike S106, it has no HII region, compact or otherwise. This places it distinctly in a much earlier spot on the formative timeline than S106. Orion source 1 is a textbook example of a young, forming massive star.

Mature HII regions are observed during much later stages of stellar formation. In contrast to Orion-KL and Orion source 1, mature HII regions represent the opposite end of the evolutionary timeline for forming stars. An excellent example for a mature HII region is the Trapezium in the Orion nebula. Located in the core of the Orion nebula, the trapezium is a group of young OB stars responsible for a majority of the illumination of the nebula as a whole. Morphologically, none of the stars within the trapezium, although still very young, have any remaining accretion disks. Any accreting material has been entirely ablated, and any disks, destroyed. The result is a large cavity within the Orion nebula, which is effectively one large HII region. Together, these facts make the Trapezium a good example of what a fully evolved star forming region looks like. That is to say, the region is far along on the formative timeline. Another example of an ionization cavity is the center of the Rosette nebula. The Rosette nebula's cavity is much more visually apparent than that of the Trapezium in the Orion nebula, and so images of the Rosette nebula are given in figures AF and AG, in lieu of images of the Orion nebula's Trapezium.

Section 5 – Interpretation of Data

S106 IR is an incredibly active MYSO. It is PDR dominated, and therefore well past both the protostar and adiabatic stages. It also has poorly collimated outflows (Fig. A). These signs

point to S106 IR being a class I YSO, yet, as was mentioned in section 4.1, with class I YSOs we expect to see a decrease in stellar wind driving power and a lessening disk; the consistently large proper motions (Table 2, Appendix A) within S106's lobes counteract any claims towards defining S106 IR as a class I YSO. Furthermore, the dark lane (Fig. D) may be feeding the circumstellar disk.

It is obvious S106 IR does not lie well within standard classifications. The fact that S106 has such a large expanding HII region may further suggest that S106 IR is a proper mature star that retained its younger features, though such would violate the basic definitions of "mature stars." Also peculiar are S106 FIR's water masers, a signature feature of class 0 YSOs and therefore a young stellar nursery. A young stellar nursery would not have such a highly evolved HII region.

Briefly, it is also important to recall S106 IR's deep obscurity in the optical spectrum, a trait indicative of HC+UCHII regions.

With all the latter in mind, it seems reasonable to believe S106 IR is in a transitionary phase. The amalgamation of multiple distinctive traits characteristic of separate, known, formative stages is certainly suggestive of such a state.

Additionally, the observed characteristics of the S106 nebula lend themselves to three possible models that describe S106's morphology: [1] The central star, S106 IR, may have experienced an explosion a few millennia ago that initiated the nebular motions. [2] The nebular motions may be associated with a dense expanding shell produced by stellar winds. [3] The evolving nebula consists of recently ionized ejecta launched during a bipolar-molecular outflow

phase during accretion. With the analysis presented in section 3, a potential model may be chosen.

From the S&R data, it seems the highest radial velocities and greatest line-widths and line splitting are confined to within 30” of S106 IR. Outside 30” from S106 IR, radial velocities are low; however, proper motions continue to increase. This suggests that within R < 30”, stellar wind from S106 IR has carved out a cavity (Fig. AH). At ~30”, a height fragmented shell is traced by the brightest emission, depicted in figure AI, in the HST images.

Fig. AH: Carved-out Cavities of Sharpless 2-106

The cavity carved out by Sharpless 2-106’s stellar wind is very distinctly represented in this image, and somewhat resembles a pill shape. The relative size difference between the carved-out cavity and the lobes on which the presented velocity analysis was preformed is also well demonstrated in this image.

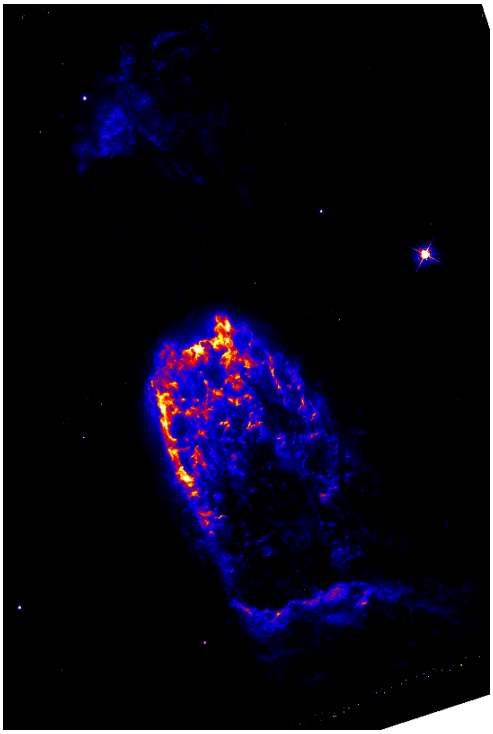

Fig. AI: Brightest Emission of Sharpless 2-106

The brightest emission from the HST Sharpless 2-106 images is highlighted here.

This shell may suggest model [2]. As can be seen in Table 2, the proper motions of the S106 nebula increase with distance from the ionizing source. Velocity vectors projected onto a 2D plane from a 3D expanding spherical shell exhibit this same behavior (Fig. AJ), hence the mention of this model. Unlike the proper motions, however, the radial velocities of such a shell increase with proximity to the ionizing source, assuming the center of the geometrical projection lies along the line of sight. This behavior is not present in the data. Instead, both the nebular proper motions *and* radial velocities are observed to increase with distance from the ionizing source. Because of this, model [2] may be ruled out. Additionally, the $V > 100$ kms^{-1} motions cannot be driven by thermal pressure gradients, and the current stellar wind does not appear to reach this far.

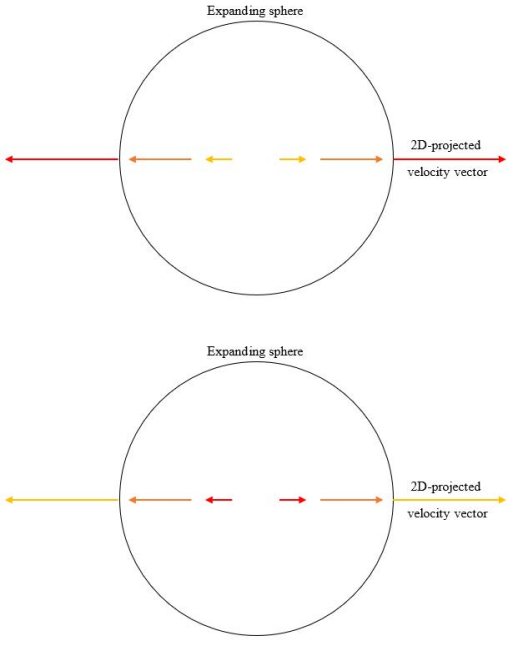

Fig. AJ: Spherical Velocity Projections

A depiction of velocity vectors corresponding to the surface of an expanding sphere, projected onto a 2D diagram. The velocity vectors in both diagrams may equivalently correspond to observed motions of matter. The bottom diagram is the same model as the top, rotated 180 degrees. As can be seen, the red vectors, which were at a maximum perceived value in the top orientation, have decreased in magnitude, as the angle from the line of sight has been decreased from 90° to nearly parallel.

In the case of the selected regions or "gaseous clumps" chosen in Sharpless 2-106's primary lobes, motions caused by this sort of expansion would result in proper motions that increase with distance from the center, and radial motions that decrease with distance from the center, if observed along a line of sight to the center.

This leaves models [1] and [3] – an explosion, or a newly ionized fossil bipolar outflow wall. To observe an increasing velocity in motions from bipolar emission, the emission must be shaped relative to the line of sight in just the right way. There would need to be a bend in the general structure, with the walls towards the ends of the bipolar structure ending more parallel to the plane of the sky than the middle. Regardless of bend, however, if the apparent cylindrical geometry in the HST images is assumed, similar proper motions between gas along each wall, respective of lobe, at equal distances from the ionizing source would be expected. This is not reflected in the data. Instead, the measured proper motions increase across the width of the southern lobe, from right to left, and similarly, increase across the width of northern lobe, from left to right (both in addition to overall, with distance from the ionizing source). This exact pattern is also seen in the radial velocity data. This leaves the explosion model as the most likely.

It is thought that if there was an explosion, this may also suggest the explosion itself was bipolar in nature, and tilted slightly away from the axis of the lobes, creating the differential motion patterns seen across the lobes (Fig. AK). Additionally, some aspects of the morphology present in S106 are not unlike those of the Orion OMC1 explosion. Orion OMC1 is the result of an explosion thought to have taken place ~500 years ago. The explosion left behind gaseous high-velocity outflow structures (streamers) that resemble “fingers”. Similar structures are found in S106, further supporting the explosion model. See figures AL and AM for the Orion OMC1 explosion, and the similar structures found in S106.

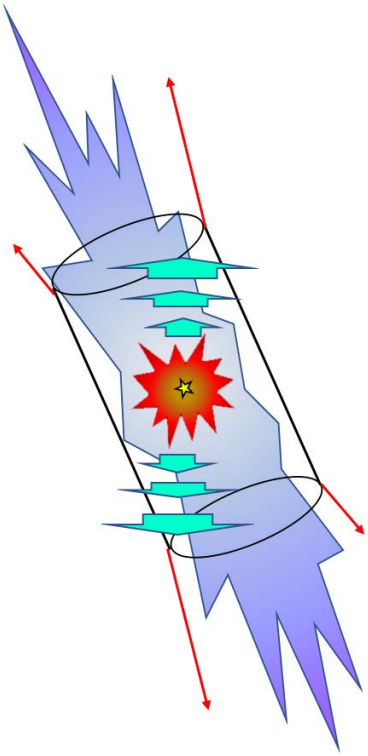

Fig. AK: Sharpless 2-106 Explosion Model

A model for the explosion that likely occurred in S106 a few millennia ago.
The cylinder represents the suspected cylindrical geometry of the bipolar emission. The purple shape represents the newly ionized fossil bipolar outflow. The yellow star represents S106 IR. The red explosion represents the explosion. The cyan arrows represent the general direction of the brunt of the explosion. The red line-arrows represent and depict the observed differential proper motion pattern across each lobe.

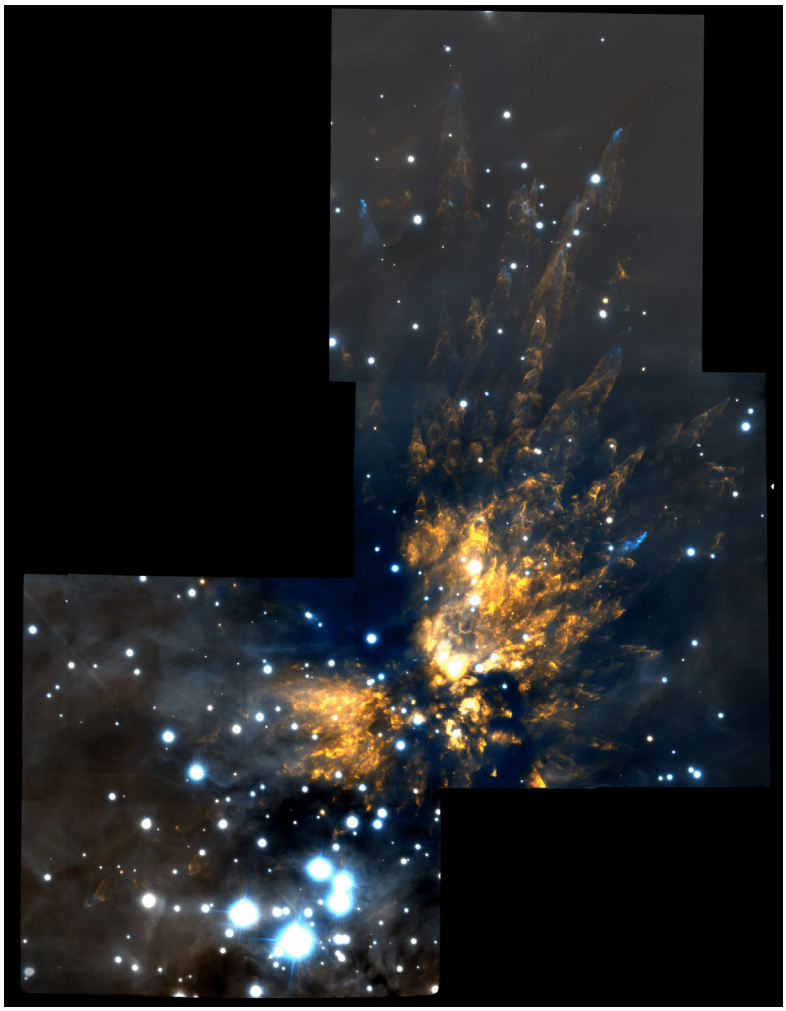

Fig. AL: The Orion OMC1 Explosion

(Bally et al. 2015)

Wide-field image of the OMC1 outflow in H_2 (orange) and [FeII] (cyan). The finger-like streamers are the result of an explosion that is thought to have occurred roughly 500 years ago.

Fig. AM: Structures in Sharpless 2-106 Similar to those found in Orion OMC1

In the three figures to the right, streamer-like structures of gas in Sharpless 2-106 that are similar to those found in Orion OMC1 are highlighted. The top image is the northern lobe. The middle and bottom images are of the southern bar.

Though not as "finger-like" as the Orion OMC1 streamers, the structures highlighted are still distinctive of incredible motions, and were likely created as the result of an explosion, in a fashion not dissimilar to the creation of the OMC1 streamers.

Notably, the southern bar shows signs of considerable disturbance.

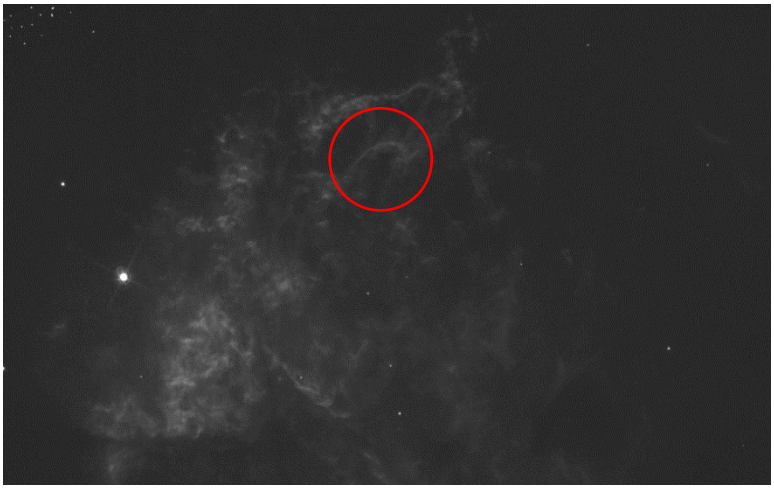

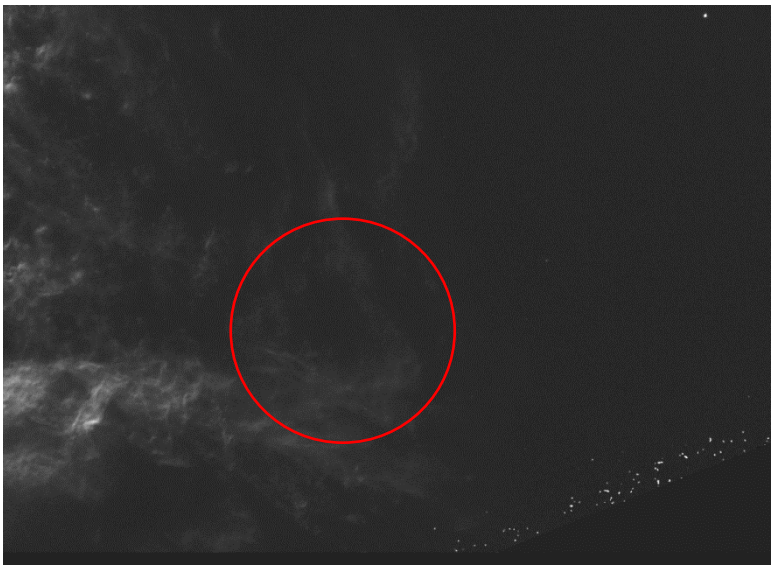

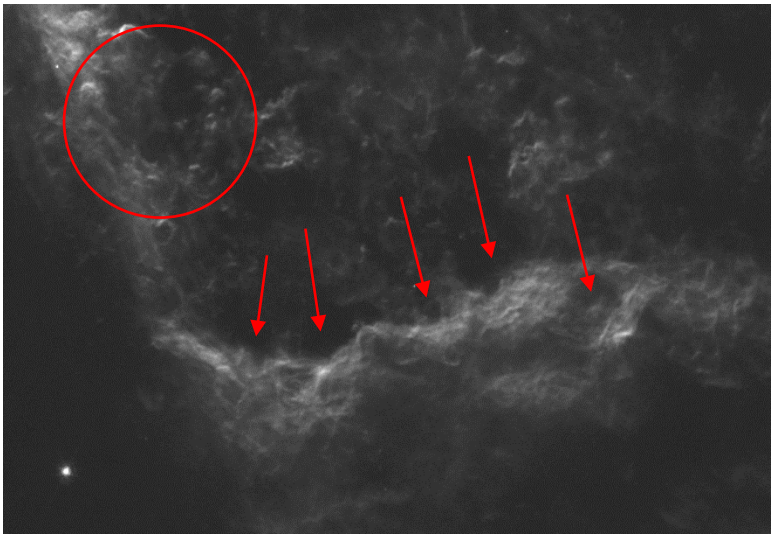

Conclusion

S106 provides a unique opportunity to study the transitionary stage from massive protostar to a mature main sequence star. The velocity analysis presented suggests S106 is in a late transitionary state, and confirms the presence of nebular proper motions many times the sound speed in photo-ionized plasma. These motions were likely caused by an explosion that occurred in the S106 nebula a few millennia ago, as evidenced by patterns within the velocity map of its primary bipolar lobe structures. Further studies on S106's morphology may yield solutions to some of the current unknowns surrounding the mechanisms of formative stellar phases, and massive star evolution.

Section 6 - Future Prospects

The analysis and study presented in this paper provide data and statistics purposeful to future studies of the S106 nebula. The velocity values found allow for the creation of more accurate models of the S106 nebula. It is hoped models utilizing the data presented here will assist in elucidating the mechanisms behind morphologies exhibited by such nebulas as S106. Further prospects include interactive 3D models as well; the current state of virtual and augmented reality systems allows for real-time interactive models to be examined in a 3D space. Using the latest data sets containing statistics like those presented by this paper in virtual and augmented reality systems may accelerate our ability to achieve full understanding of the mechanisms of high-mass star formation.

Acknowledgements

The data used was based on observations made with the NASA/ESA Hubble Space Telescope, and obtained from the Hubble Legacy Archive, which is a collaboration between the Space Telescope Science Institute (STScI/NASA), the European Space Agency (ST-ECF/ESAC/ESA) and the Canadian Astronomy Data Centre (CADC/NRC/CSA). Some/all of the data presented in this paper were obtained from the Mikulski Archive for Space Telescopes (MAST). STScI is operated by the Association of Universities for Research in Astronomy, Inc., under NASA contract NAS5-26555. This work has made use of data from the European Space Agency (ESA) mission Gaia (https://www.cosmos.esa.int/gaia), processed by the Gaia Data Processing and Analysis Consortium (DPAC, https://www.cosmos.esa.int/web/gaia/dpac/consortium). Funding for the DPAC has been provided by national institutions, in particular the institutions participating in the Gaia Multilateral Agreement.

Special thanks are extended to the following individuals:

Dr. John Bally, for his guidance over the last few years and support in my undertaking of the thesis process.

Dr. Ann-Marie Madigan, for her instruction and advice regarding writing a thesis.

Dr. Harrison Stalvey, for his invaluable support and patience with me when he was my professor, and over the last couple of semesters.

Additionally, The University Brand Identity Standards Board is thanked for granting me permission to use the official University of Colorado commercial seal on the cover page of this paper.

I would like to extend much gratitude as well to all my peers from the last four years. Their moral support has aided me tremendously.

Lastly, I would like to thank my Mom and Dad for always being there, and providing so much affection over the years. Without their support, there is little doubt in my mind I would not be where I am today.

References

Anderson, L D, et al. "The Molecular Properties of Galactic H II Regions." *The Astrophysical Journal Supplement Series* 181 (2009): 255-271.

Bally, J, R L Snell and R Predmore. "Radio images of the bipolar HII region S 106." *The Astrophysical Journal* 272 (1983): 154-162.

Bally, John, et al. "*Hubble Space Telescope* Wide Field Planetary Camera 2 Observations of the Young Bipolar H_{ii} Region S106." *The Astronomical Journal* 116.4 (1998): 1868-1881.

—. "The Orion fingers: Near-IR adaptive optics imaging of an explosive protostellar outflow." *Astronomy and Astrophysics* 579 (2015): A130.

Balsara, D, D Ward-Thompson and R M Crutcher. "A turbulent MHD model for molecular clouds and a new method of accretion on to star-forming cores." *Monthly Notices of the Royal Astronomical Society* 327.3 (2001): 715-720.

Bonnell, Ian A, Matthew R Bate and Hans Zinnecker. "On the formation of massive stars." *Monthly Notices of the Royal Astronomical Society* 298.1 (1998): 93-102.

Breen, Shari L and Simon P Ellingsen. "Masers as evolutionary tracers of high-mass star formation." *Cosmic Masers - from OH to H0*. 2012. 156-160.

Churchwell, Ed. "Ultra-Compact HII Regions and Massive Star Formation." *Annual Review of Astronomy and Astrophysics* 40 (2002): 27-62.

Collaboration, Gaia, et al. "Gaia Data Release 2. Summary of the contents and survey properties." *Astronomy and Astrophysics* 616 (2018): A1.

—. "The Gaia mission." *Astronomy and Astrophysics* 595 (2016): A1.

Comerón, F, et al. "The ionizing source of the bipolar HII region S106: A close massive binary." *Astronomy and Astrophysics* 615 (2018): A2.

D. Padgett (IPAC/Caltech), W. Brandner (IPAC), K. Stapelfeldt (JPL), NASA. "IRAS 04302+2247." *I04302*. NASA, 9 February 1999. <https://hubblesite.org/contents/media/images/1999/05/767-Image.html?news=true>.

Deharveng, L, et al. "A gallery of bubbles. The nature of the bubbles observed by Spitzer and what ATLASGAL tells us about the surrounding neutral material." *Astronomy and Astrophysics* 523 (2010): A6.

Furuya, Ray S, et al. "VLA Observations of H_2O Masers in the Class 0 Protostar S106 FIR: Evidence for a 10 AU Scale Accelerating Jetlike Flow." *The Astrophysical Journal* 525 (1999): 821-831.

Gibb, A G and M G Hoare. "A high-frequency radio continuum study of massive young stellar objects." *Monthly Notices of the Royal Astronomical Society* 380.1 (2007): 246-262.

Goldman, Don. *Nebula*. n.d. <https://astrodonimaging.com/>.

Greene, Thomas P. "Protostars: "Stellar embryology" takes a step forward with the first detailed look at the youngest Sun-like stars." *American Scientist* 89.4 (2001): 316-325.

Hoare, M G and T B Muxlow. "MERLIN Observations of Luminous Young Stellar Objects." Hoare, M G and T B Muxlow. *Radio Emission from the Stars and the Sun*. Vol. 93. 1996. 47.

Hoare, M G, et al. "Ultracompact Hii Regions and the Early Lives of Massive Stars." *Protostars and Planets V*. 2007. 181.

Hodapp, K W and N Schneider. "S106." Hodapp, K W and N Schneider. *Handbook of Star Forming Regions, Volume I*. Vol. 4. 2008. 90.

Hodapp, Klaus-Werner and John Rayner. "The S106 Star-Forming Region." *The Astronomical Journal* 102 (1991): 1108.

Hosokawa, Takashi and Kazuyuki Omukai. "Evolution of Massive Protostars with High Accretion Rates." *The Astrophysical Journal* 691 (2009): 823-846.

Keto, Eric. *Smithsonian Astrophysicsal Observatory Submillimeter Array*. 18 February 2020. <https://www.cfa.harvard.edu/sma/research/StarFormation/MassiveStar/HighMassResearch/>.

Lada, Charles J. "Star formation: from OB associations to protostars." *Star Forming Regions*. 1987. 1.

Lee, Chin-Fei, et al. "First detection of equatorial dark dust lane in a protostellar disk at submillimeter wavelength." *Science Advances* 3 (2017): e1602935.

M.R. Haneveer. "Orbital Lifetime Predictions: An assessment of model-based ballistic coefficient estimations and adjustment for temporal drag coefficient variations." Delft University of Technology, 2017.

Maud, L T, et al. "A distance-limited sample of massive star-forming cores from the RMS★ survey." *Monthly Notices of the Royal Astronomical Society* 452.1 (2015): 637-655.

Max Planck Gesellschaft. *Abteilung Planeten- und Sternentstehung*. 2020. <https://www.mpia.de/de/abteilung-psf>.

Motte, F, P Andre and R Neri. "The initial conditions of star formation in the rho Ophiuchi main cloud: wide-field millimeter continuum mapping." *Astronomy and Astrophysics* 336 (1998): 150-172.

NASA. "Orion Nebula." *New Hubble image of Kleinmann-Low Nebula*. European Space Agency/Hubble, 17 March 2017. <https://www.spacetelescope.org/images/heic1705a/>.

Oasa, Yumiko, et al. "Very Low Luminosity Young Cluster and the Luminosity and Mass Functions in S106." *The Astronomical Journal* 131 (2006): 1608-1628.

Peters, Thomas, et al. "Limiting Accretion onto Massive Stars by Fragmentation-induced Starvation." *The Astrophysical Journal* 725 (2010): 134-145.

Schneider, N, et al. "Anatomy of the massive star-forming region S106. The [O I] 63 μm line observed with GREAT/SOFIA as a versatile diagnostic tool for the evolution of massive stars." *Astronomy and Astrophysics* 617 (2018): A45.

Sinnott, R W. "Virtues of the Haversine." *Sky and Telescope* 68 (1984): 158.

Solf, J and U Carsenty. "The kinametical structure of the bipolar nebula S 106." *Astronomy and Astrophysics* 113 (1982): 142-149.

Stahler, Steven W., Palla Francesco and Paul Tseng-Pu Ho. "The Formation of Massive Stars." *Protostars and Planets*. Ed. A.P. Boss, S.S. Russell V. Mannings. IV. Tucson: University of Arizona Press, 2000. 327-51.

Trefzger, Ch. and J Solf. "Calibration of spectrograms using a Lyot filter element." *Astronomy and Astrophysics* 63 (1978): 131-136.

Vallée, Jacques P and Jason D Fiege. "A Cool Magnetized Shell Wrapped around the Hot H II Region S106: Geometry, Kinematics, Magnetic Vectors, and Pressure Balance." *The Astrophysical Journal* 627 (2005): 263-276.

van den Ancker, M E, A G G M Tielens and P R Wesselius. "ISO Spectroscopy of the young bipolar nebulae S106 IR and Cep A East." *Astronomy and Astrophysics* 358 (2000): 1035-1048.

Vaytet, Neil, et al. "Simulations of protostellar collapse using multigroup radiation hydrodynamics. II. The second collapse." *Astronomy and Astrophysics* 557 (2013): A90.

Xu, Y, et al. "On the Nature of the Local Spiral Arm of the Milky Way." *The Astrophysical Journal* 769 (2013): 15.

Zinnecker, Hans and Harold W Yorke. "Toward Understanding Massive Star Formation." *Annual Review of Astronomy and Astrophysics* 45 (2007): 481-563.

Zucker, Catherine, et al. "A Large Catalog of Accurate Distances to Local Molecular Clouds: The Gaia DR2 Edition." *The Astrophysical Journal* 879 (2019): 125.

Appendix A:

Table 2. Region Velocity Values

#	Tangential V (kms^{-1})	Radial V (kms^{-1})	True V (Mag.) (kms^{-1})
	South Lobe		
1.	72.8	-20.325	75.6
2.	42.8	9	43.7
3.	47.1	3.75	47.2
4.	34.1	1.5	34.1
5.	25.9	0	25.9
6.	36.5	0	36.5
7.	94.8	5.625	95.0
8.	42.6	-13.125	44.6
9.	40.3	15	43.0
10.	27.9	-3.75	28.2
11.	56.6	-5	56.8
12.	61.4	2.5	61.5
13.	59.8	-1.875	59.8
14.	44.2	9	45.1
15.	64.1	-11.25	65.1
16.	59.3	-6.25	59.6
17.	38.9	7.5	39.6
18.	39.3	0	39.3
19.	56.3	-33.75	65.6
20.	84.1	20	86.4
21.	49.4	0	49.4
22.	39.8	-6	40.2
23.	49.4	2.5	49.5
24.	32.5	-49.5	59.2
25.	76.2	-17.5	78.2
26.	55.9	-7.5	56.4
27.	35.7	6.25	36.2
28.	79.7	-3.75	79.8
29.	43.9	-28.125	52.1
30.	66.9	-16.5	68.9
31.	58.3	-3	58.4
32.	63.3	9.375	64.0
33.	46.4	11.25	47.7
34.	66	30	72.5
35.	54.8	-16.875	57.3

Key:

Red regions roughly split S106 and its lobe structures along their length.

Orange regions lay in-between the red regions and the edges of S106 and its lobe structures.

Yellow regions lie along the edges of S106 and its lobe structures.

36.	99	-4.5	99.1
37.	50	10.5	51.1
38.	55.9	9.375	56.7
39.	72.6	15	74.1
40.	50.7	-18	53.8
41.	91.7	-7.5	92.0
42.	80.7	N/A	N/A
43.	60.6	3.75	60.7
44.	64.2	40	75.6
45.	96.9	40	104.8
46.	58.3	3	58.4
47.	91.8	N/A	N/A
48.	59.7	1.875	59.7
49.	98.1	7.5	98.4
50.	86.3	42	96.0
51.	97.6	1.5	97.6
	South bar		
52.	47.1	N/A	N/A
53.	122.5	N/A	N/A
54.	65.7	-1.875	65.7
55.	83.1	3.75	83.2
56.	64.5	N/A	N/A
57.	50	N/A	N/A
58.	52.3	0	52.3
59.	47.2	0	47.2
60.	54.9	3.75	55
61	56.9	N/A	N/A
62.	63.8	N/A	N/A
63.	56.3	0	56.3
64.	47.4	-1.875	47.4
65.	72.1	N/A	N/A
66.	57.2	N/A	N/A
	North Lobe		
67.	8.5	11.25	14
68.	28.6	26.25	38.8
69.	30.4	22.5	37.8
70.	10.3	16.25	19.2
71.	20.4	N/A	N/A
72.	21.7	17.5	27.9
73.	31.8	24.375	40.1
74.	28.6	20.625	35.3
75.	43.4	N/A	N/A
76.	61	N/A	N/A

Table 3. Proper Motions of Distinctive Clumps		
#	Tangential V (kms^{-1})	Comments
	South Lobe	
1.	86.2	SW; Near DR2 star
2.	92.0	SSW
3.	112.1	SSW
4.	12.1	SW edge
5.	119.6	Fast, isolated knot
6.	125.8	Bow in SSW corner
7.	96.6	In interior of S lobe
8.	92.1	In interior of S lobe
9.	86.2	Reverse bow near E edge
10.	62.4	On E edge
11.	90.3	Bow beyond SE edge
12.	125.9	knot in center of S lobe
13.	59.3	Head of cometary structure
14.	18.5	reverse-bow on SW edge
15.	37.2	reverse bow at wind-interface
16.	62.4	Knot on S-lobe axis
	North Lobe	
17.	39.3	Knot in N-lobe
18.	82.4	Knot at north end of N-lobe
19.	120.3	knot in N-lobe
20.	41.6	knots in bow-shaped filament
21.	63.1	knot on NE-side of N-lobe
22.	52.6	HH from S106 FIR
23.	112.2	New HH
	South Bar	
24.	26.5	South bar west
25.	73.5	South bar center bow
26.	57.9	Beyond South bar bow
27.	41.4	Beyond South bar bow east
28.	37.6	Beyond South bar knot east
29.	34.5	Bar South, bright knot
30.	50.7	Bar South, bright knot

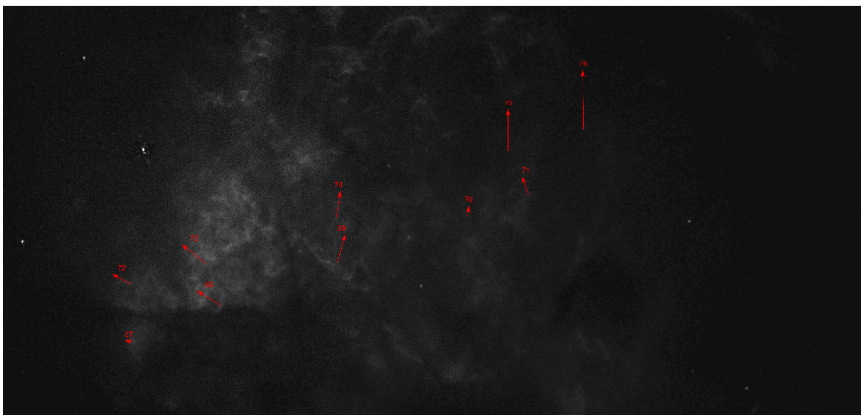

Fig. T (Left): Primary Sharpless 2-106 400-Year Scaled Vel. Vectors (Northern Regions)

Here can be seen the selected primary regions of the northern lobe of Sharpless 2-106, with velocity vectors scaled to motions over 400 years.

Fig. U (Below): Primary Sharpless 2-106 400-Year Scaled Vel. Vectors (Southern Regions)

Here can be seen the selected primary regions of the southern lobe and bar of Sharpless 2-106, with velocity vectors scaled to motions over 400 years.

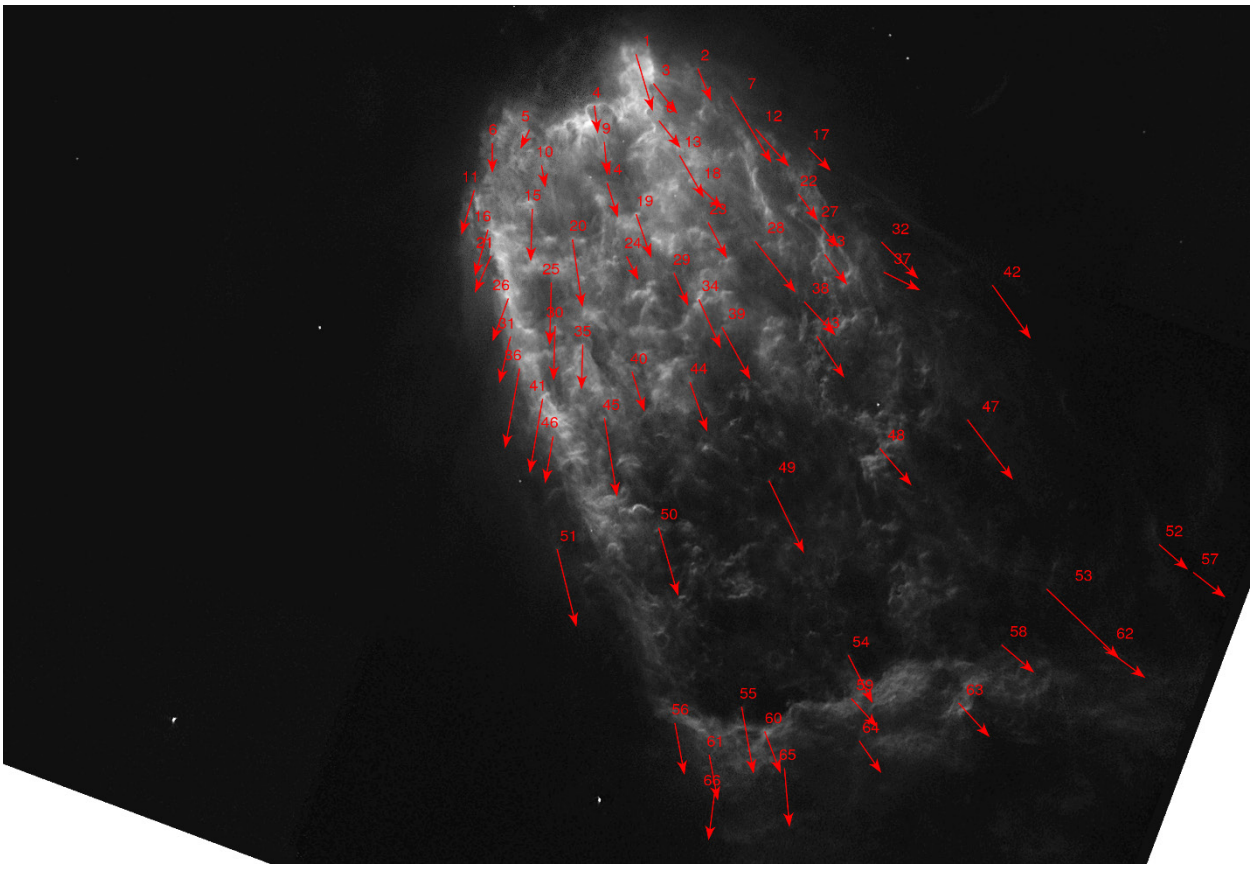

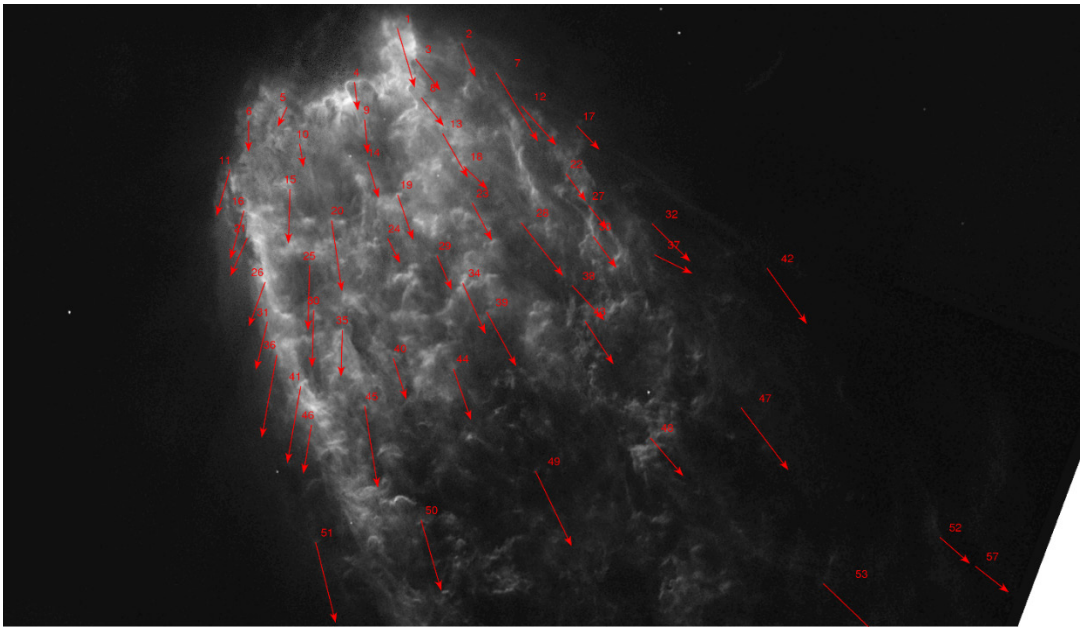

Fig. V (Above): Primary Sharpless 2-106 400-Year Scaled Vel. Vectors (Southern Lobe Regions)

Here can be seen the selected primary regions of the southern lobe of Sharpless 2-106, with velocity vectors scaled to motions over 400 years.

Fig. W (Below): Primary Sharpless 2-106 400-Year Scaled Vel. Vectors (Southern Bar Regions)

Here can be seen the selected primary regions of the southern bar of Sharpless 2-106, with velocity vectors scaled to motions over 400 years.

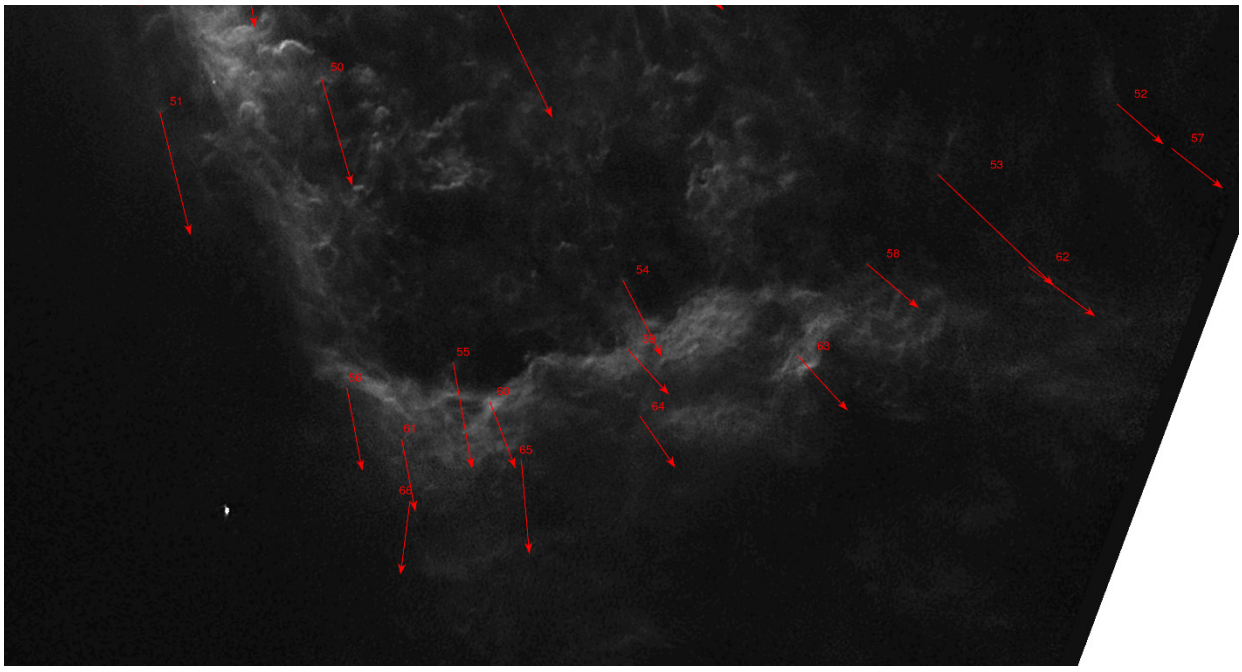

Fig. X (Right): Secondary Sharpless 2-106 400-Year Scaled Vel. Vectors (Northern Regions)

Here can be seen the selected secondary regions of the northern lobe of Sharpless 2-106, with velocity vectors scaled to motions over 400 years.

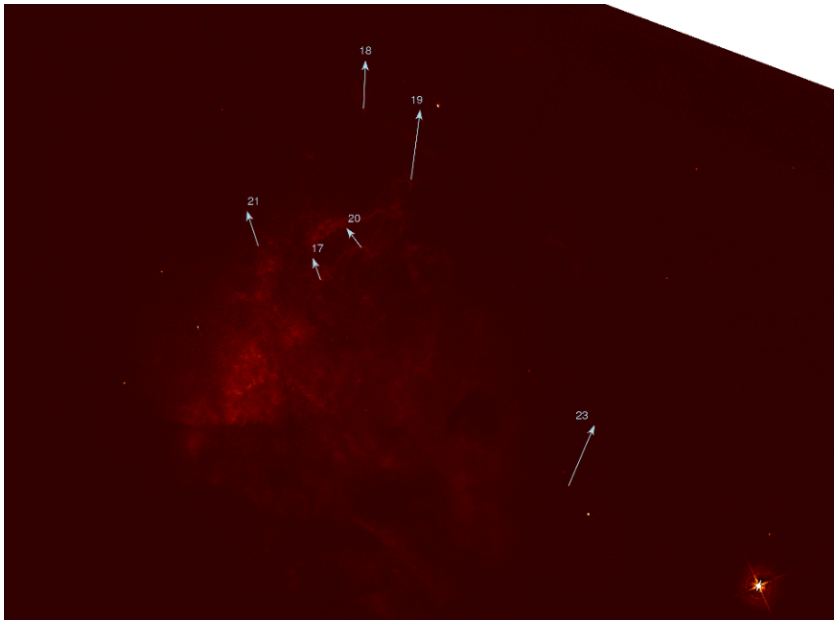

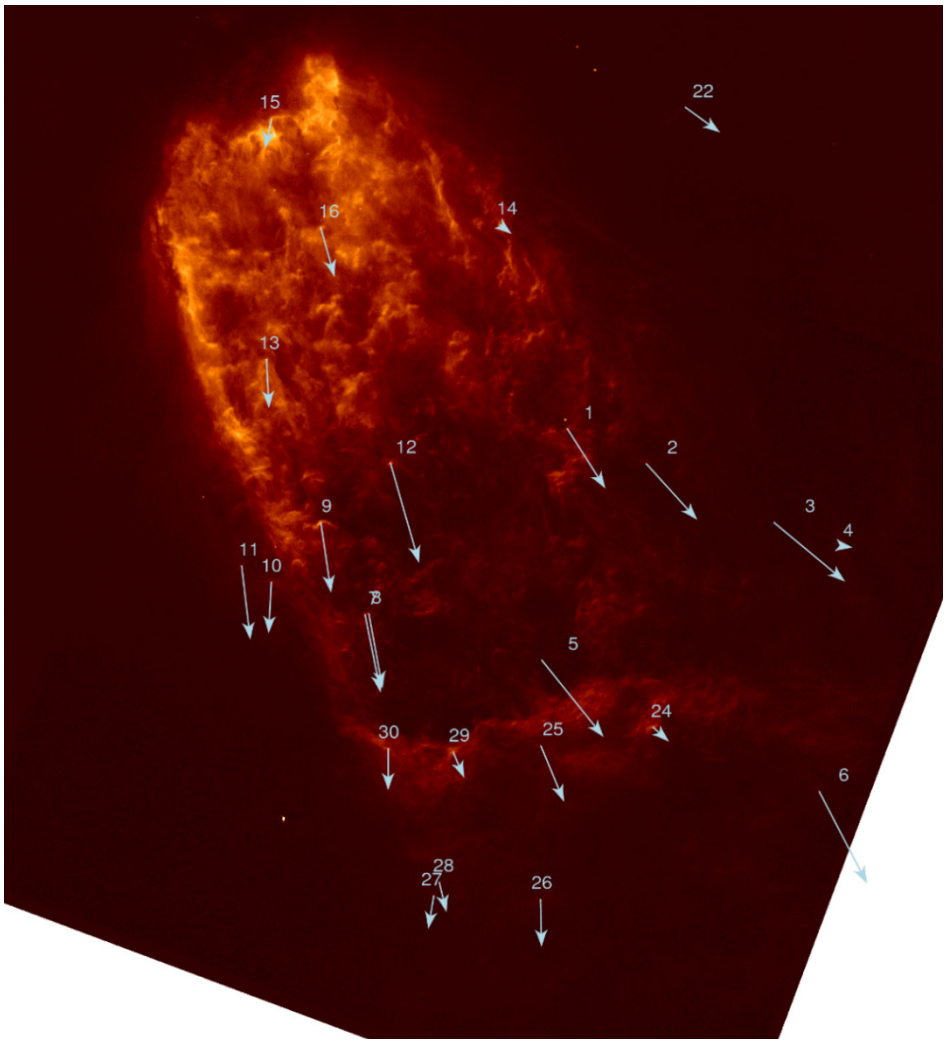

Fig. Y (Left): Secondary Sharpless 2-106 400-Year Scaled Vel. Vectors (Southern Regions)

Here can be seen the selected secondary regions of the southern lobe and bar of Sharpless 2-106, with velocity vectors scaled to motions over 400 years.

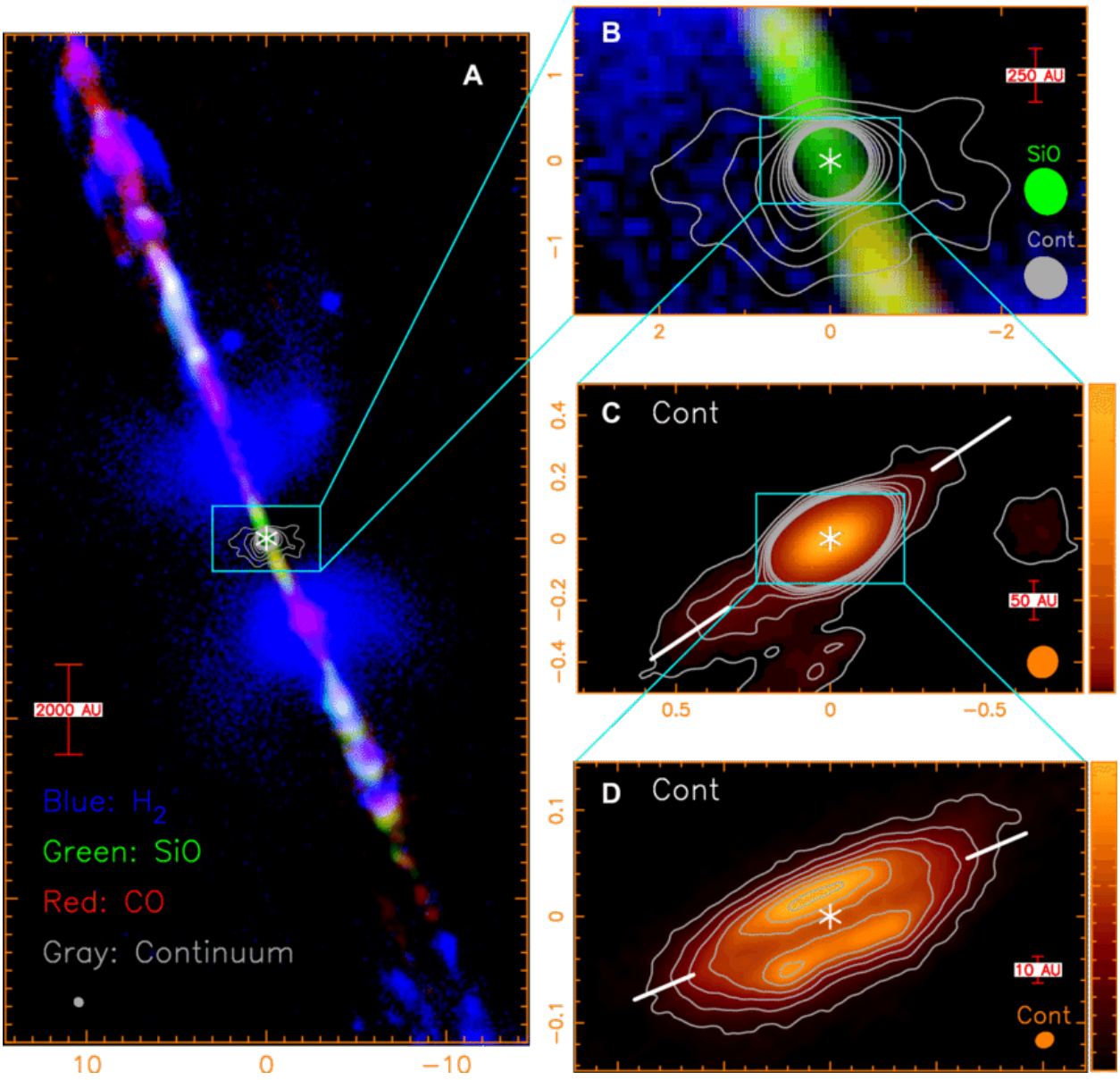

Fig. AB: HH 212

(Lee et al. 2017)

The stellar system HH 212 in H_2, SiO, CO, and continuum wavelengths.

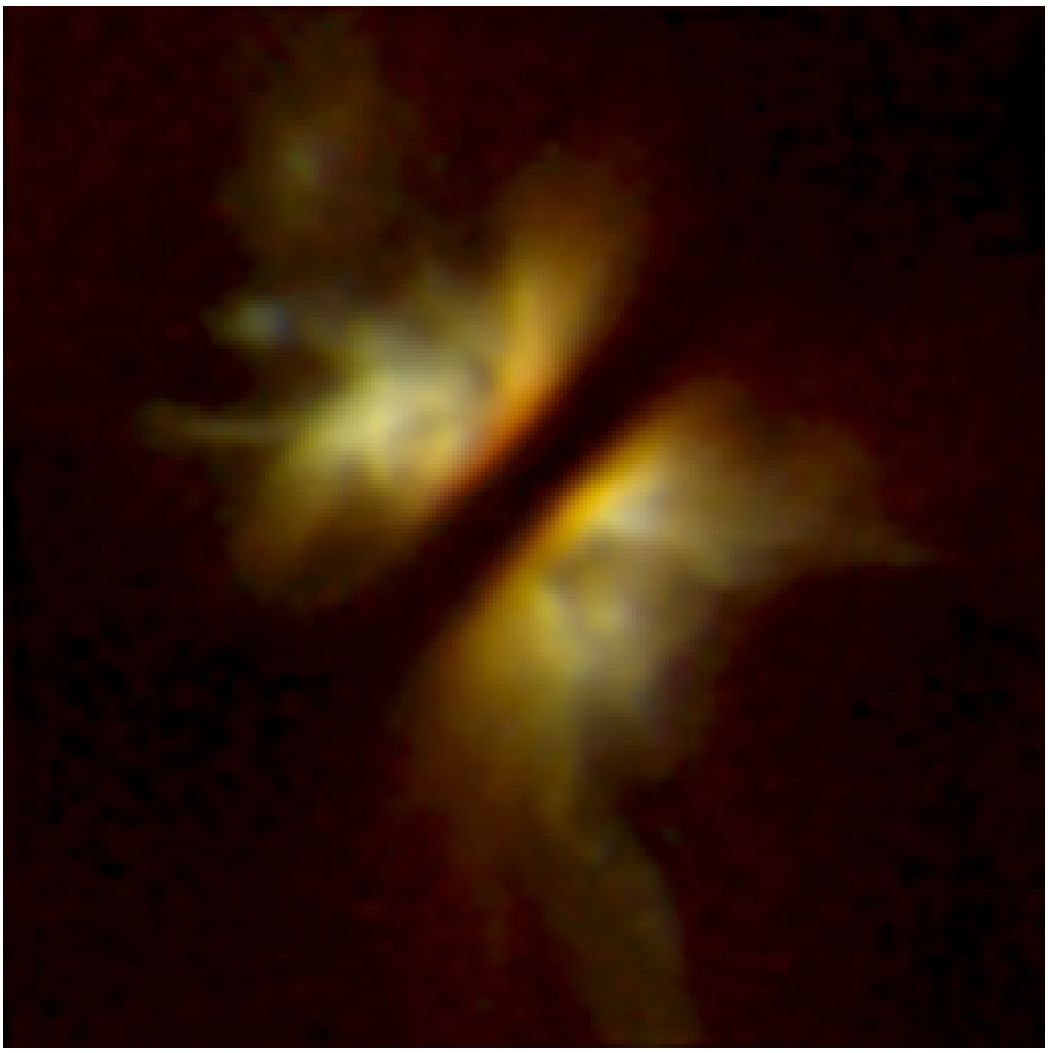

Fig. AC: The Butterfly Star (IRAS 04302+2247)

(D. Padgett et al. 1999)

The Butterfly Star (IRAS 04302+2247) is a YSO roughly 450 lightyears from Earth. As can be seen in this image, its outflows are extremely poorly columnated.

Fig. AE: Kleinmann–Low Nebula

(Nasa 2017)

An HST optical and near-infrared composite image of the Kleinmann-Low Nebula. The nebula is an extremely active star forming region.

Fig. AF: Rosette Nebula

(Goldman 2007)

The Rosette Nebula, pictured here, houses an extremely distinct ionization cavity.

Fig. AG: Rosette Nebula (Enlarged Cavity)

(Goldman 2014)

A closeup of the extremely distinct ionization cavity within the Rosette Nebula.

Appendix B:

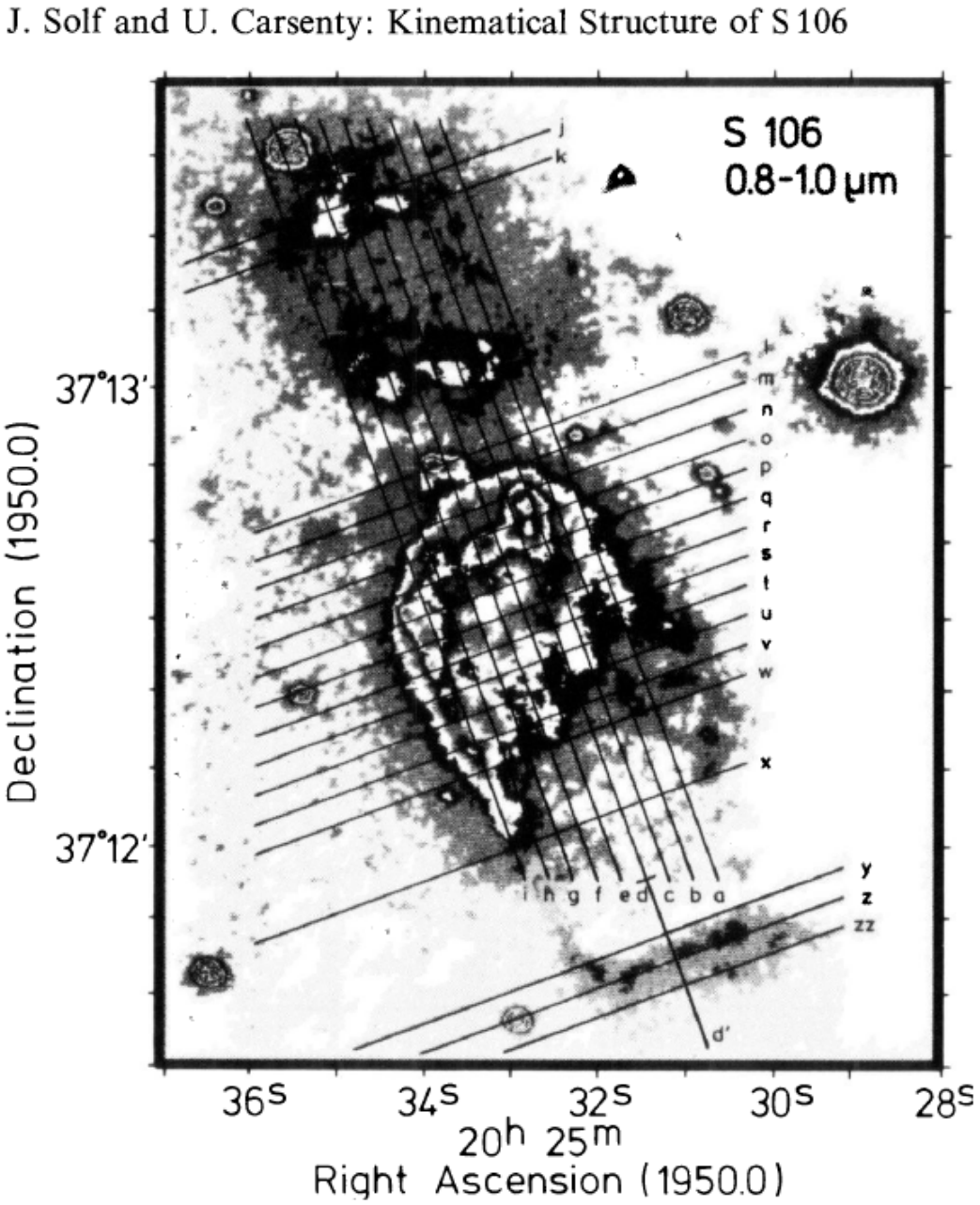

Fig. L: Solf & Carsenty Fig. 1

(Solf & Carsenty 1982)

Digitized near-infrared image tube photograph of Sharpless 2-106. The bars labeled a to zz indicate the slit positions of the coudé spectrograph observations done by Solf & Carsenty (1982).

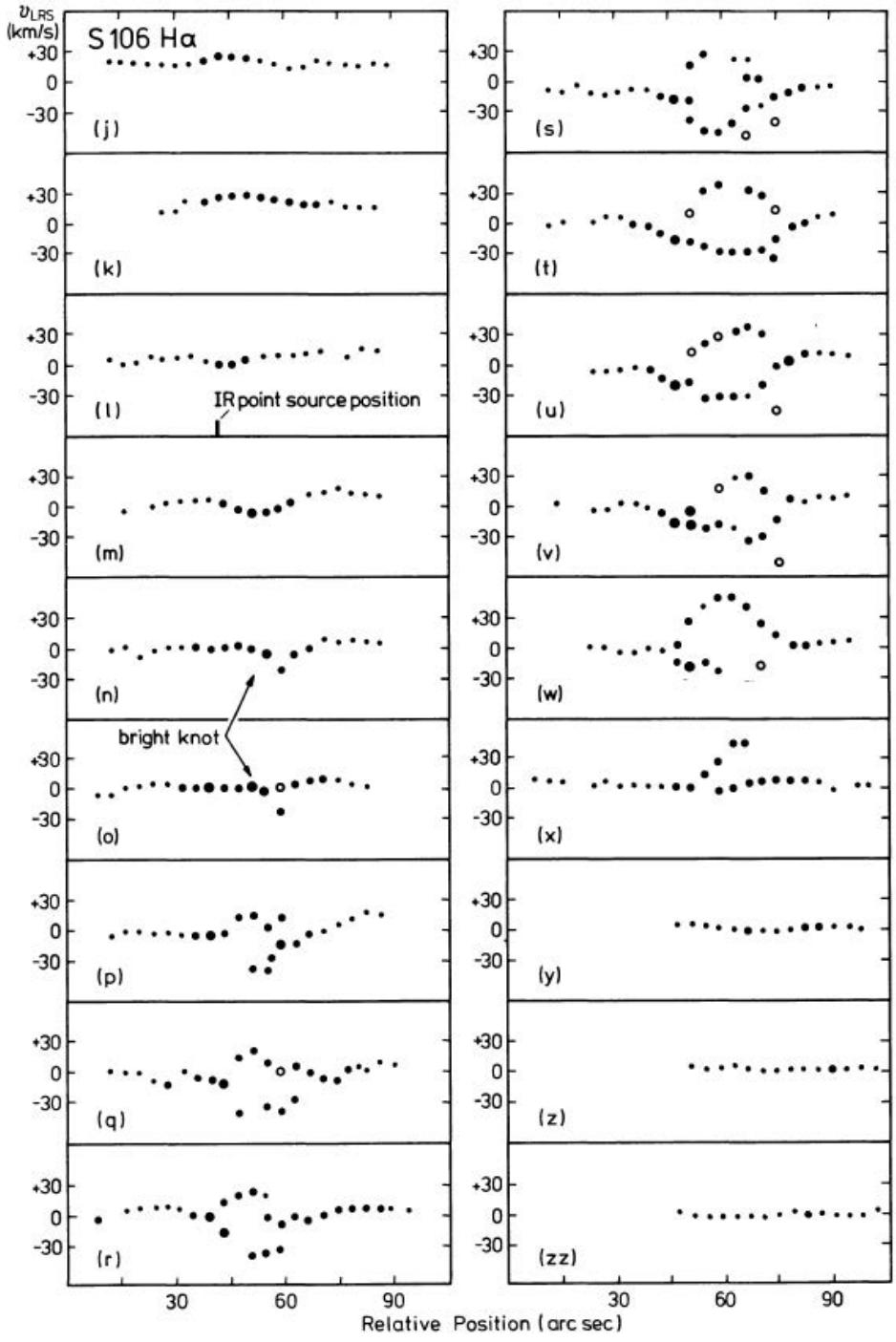

Fig. M: Solf & Carsenty Fig. 5j-zz

(Solf & Carsenty 1982)

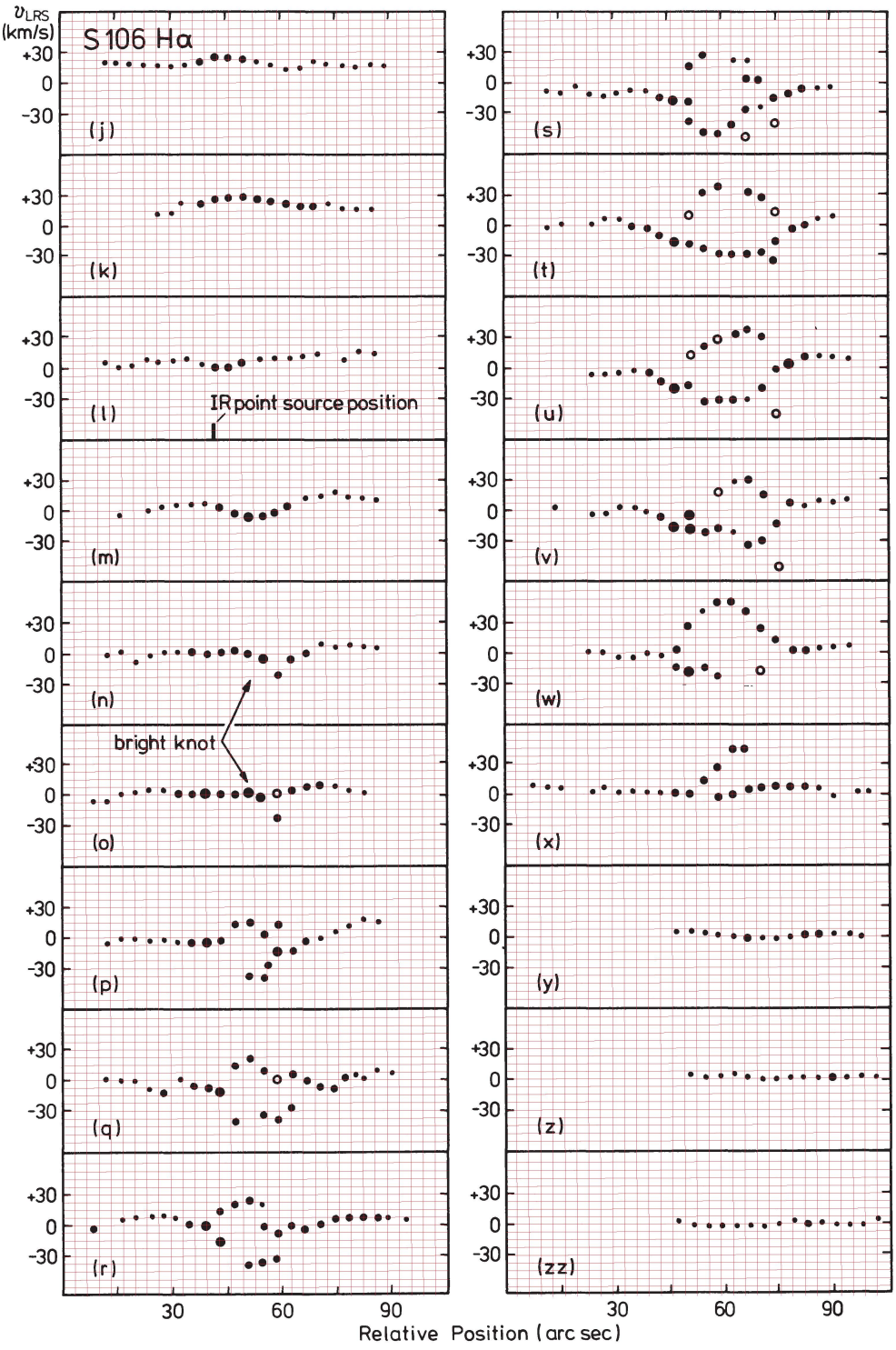

Fig. N: Solf & Carsenty Fig. 5j-zz With Divisions

(Adapted from Solf & Carsenty 1982)

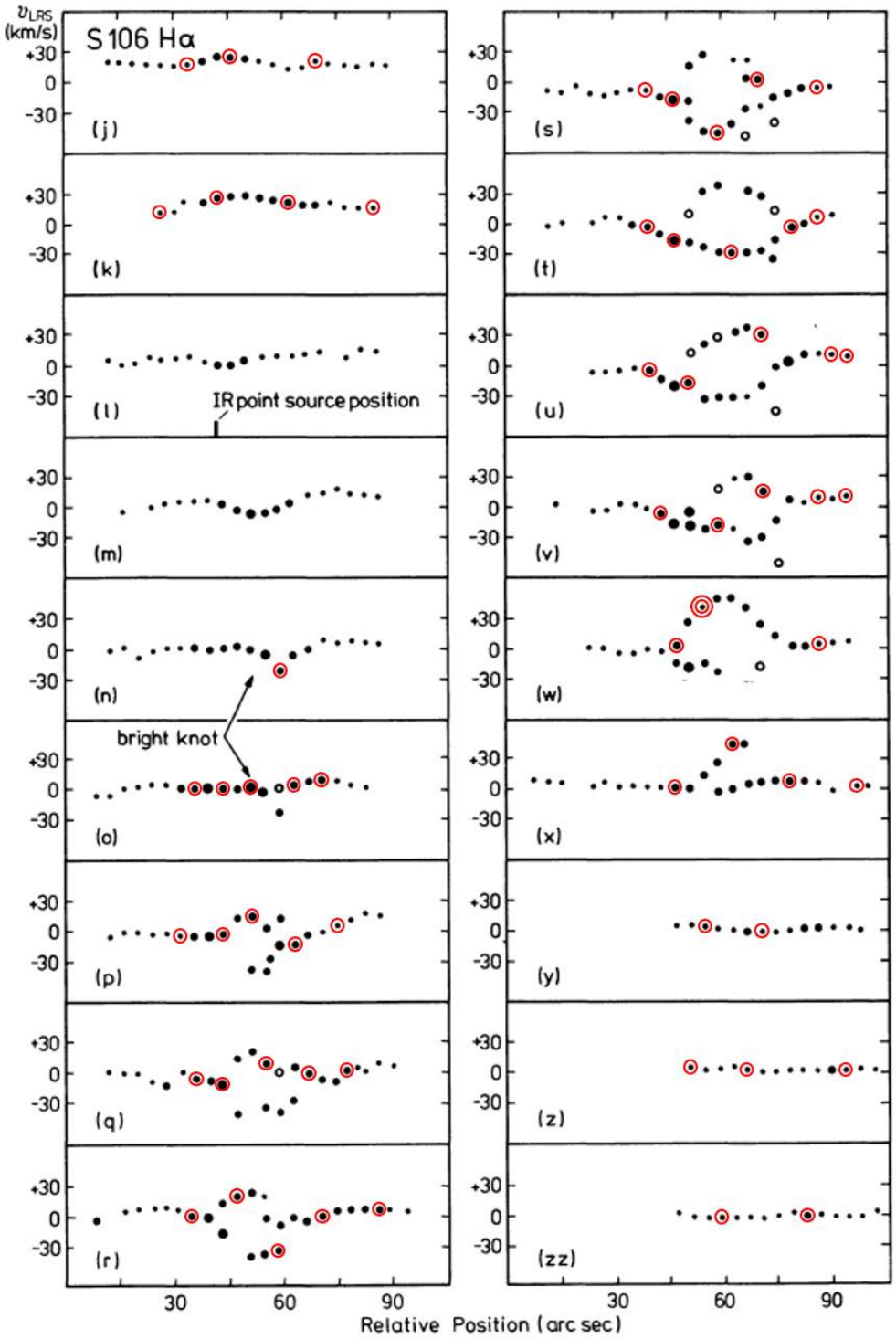

Fig. O: Solf & Carsenty Fig. 5j-zz Chosen Data Points

(Adapted from Solf & Carsenty 1982)

Table 4. Solf & Carsenty Radial Velocity Plots – Corresponding Regions to Selected Data

Radial Velocity Plot (left)						Radial Velocity Plot (right)					
(j)	72	73	74	N/A	N/A	(s)	26	25	24	23	22
(k)	67	68	69	70	N/A	(t)	31	30	29	28	27
(l)	N/A	N/A	N/A	N/A	N/A	(u)	36	35	34	33	32
(m)	N/A	N/A	N/A	N/A	N/A	(v)	41	40	39	38	37
(n)	1	N/A	N/A	N/A	N/A	(w)	46	45	44	43	N/A
(o)	6	5	4	3	2	(x)	51	50	49	48	N/A
(p)	11	10	9	8	7	(y)	N/A	55	54	N/A	N/A
(q)	16	15	14	13	12	(z)	N/A	60	59	58	N/A
(r)	21	20	19	18	17	(zz)	N/A	N/A	64	63	N/A

Figures P, Q, and R below are the three images that were used when making the physical measurements for determining which data points plotted on the S&R Fig. 5j-zz radial velocity plots should be used. The horizontal and vertical lines represent the locations of the log-slits as seen on S&R Fig. 1 (Fig. L). The blue line in figure Q intersects with the middles of long-slits l-x. The red x's are the same regions as those in figures J and K.

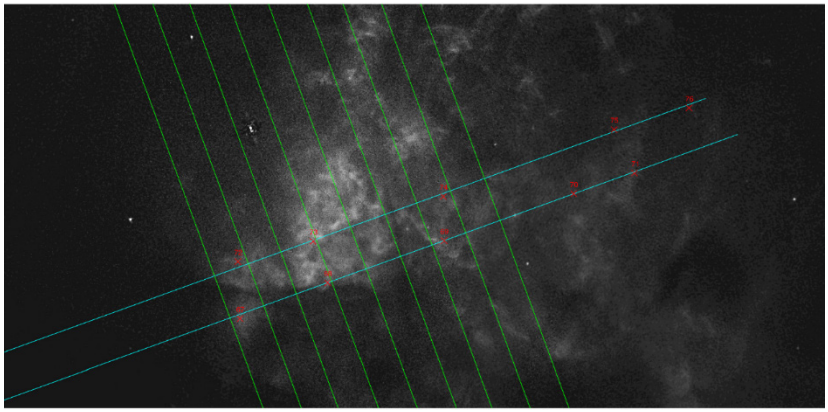

Fig. P: Sharpless 2-106 HST Image for Manual Analysis A

(Description on previous page)

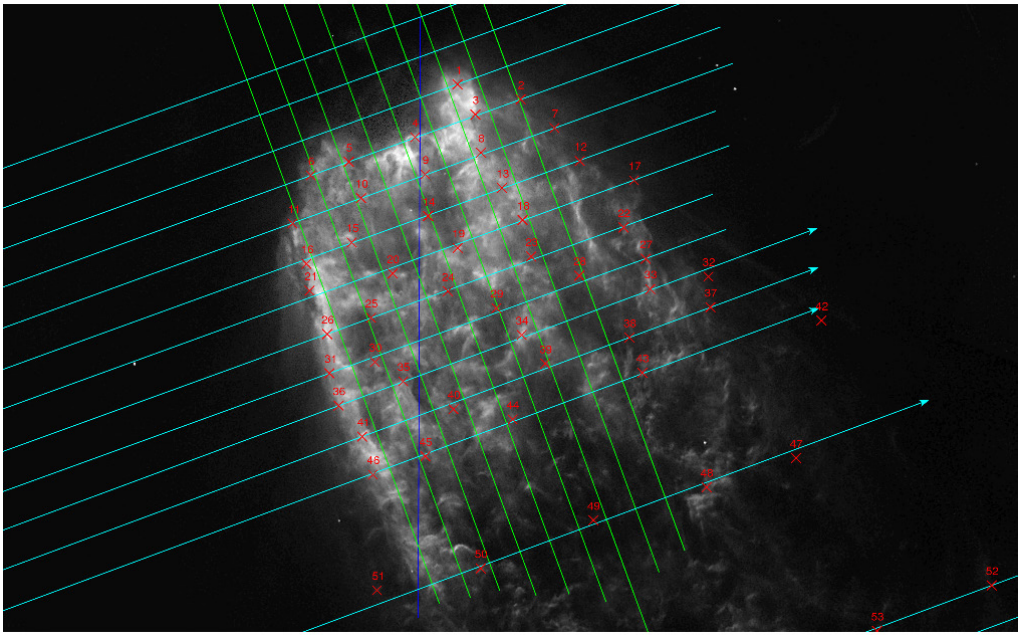

Fig. Q: Sharpless 2-106 HST Image for Manual Analysis B

(Description on previous page)

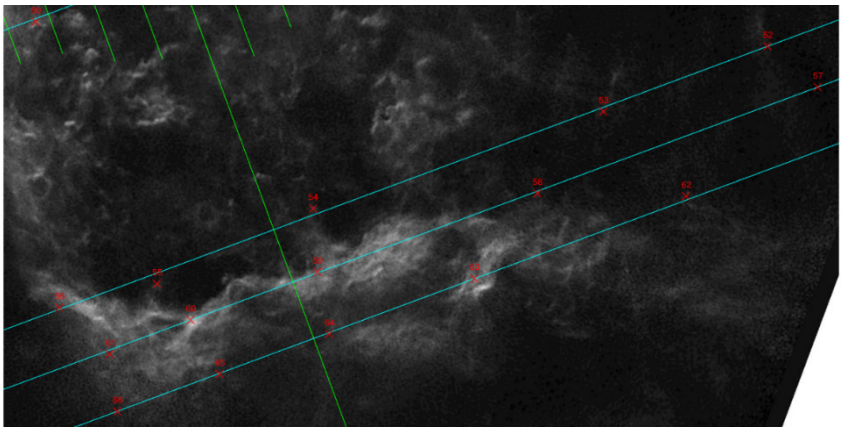

Fig. R: Sharpless 2-106 HST Image for Manual Analysis C

(Description on previous page)

Table 5. Conversion Data

#	Measured Distance from Middle of Surrogate Long-slit Reference Point (cm)	Scaled and Adjusted Distances from Corresponding S&C Fig. 1 Reference Point (cm)	Scaled and Adjusted Corresponding Distance from Middle of Radial Plot (32^{nd} divisions)	Measured Value from Radial Plot (kms^{-1})	Corresponding Tangential Velocity (kms^{-1})	Resultant True Velocity (Magnitude) (kms^{-1})
	South Lobe					
1.	1.200	0.741	1.695	-20.325	72.800	75.584
2.	3.400	2.101	4.801	9.000	42.800	43.736
3.	1.850	1.143	2.613	3.750	47.100	47.249
4.	0.200	0.124	0.282	1.500	34.100	34.133
5.	2.400	1.483	3.389	0.000	25.900	25.900
6.	3.650	2.255	5.155	0.000	36.500	36.500
7.	4.500	2.780	6.355	5.625	94.800	94.967
8.	2.050	1.267	2.895	-13.125	42.600	44.576
9.	0.200	0.124	0.282	15.000	40.300	43.001
10.	1.950	1.205	2.754	-3.750	27.900	28.151
11.	4.250	2.626	6.002	-5.000	56.600	56.820
12.	5.350	3.305	7.555	2.500	61.400	61.451
13.	2.700	1.668	3.813	-1.875	59.800	59.829
14.	0.250	0.154	0.353	9.000	44.200	45.107
15.	2.300	1.421	3.248	-11.250	64.100	65.080
16.	3.850	2.379	5.437	-6.250	59.300	59.628
17.	7.150	4.418	10.097	7.500	38.900	39.616
18.	3.400	2.101	4.801	0.000	39.300	39.300
19.	1.250	0.772	1.765	-33.750	56.300	65.641
20.	0.950	0.587	1.342	20.000	84.100	86.445
21.	3.550	2.193	5.013	0.000	49.400	49.400
22.	6.850	4.232	9.674	-6.000	39.800	40.250
23.	3.750	2.317	5.296	2.500	49.400	49.463
24.	0.950	0.587	1.342	-49.500	32.500	59.216
25.	1.600	0.989	2.260	-17.500	76.200	78.184
26.	3.050	1.884	4.307	-7.500	55.900	56.401
27.	7.550	4.665	10.662	6.250	35.700	36.243
28.	5.400	3.336	7.626	-3.750	79.700	79.788
29.	2.600	1.606	3.672	-28.125	43.900	52.137
30.	1.500	0.927	2.118	-16.500	66.900	68.905
31.	3.000	1.854	4.237	-3.000	58.300	58.377
32.	9.600	5.931	13.557	9.375	63.300	63.990
33.	7.750	4.788	10.944	11.250	46.400	47.744
34.	3.400	2.101	4.801	30.000	66.000	72.498
35.	0.500	0.309	0.706	-16.875	54.800	57.339
36.	2.700	1.668	3.813	-4.500	99.000	99.102
37.	9.800	6.055	13.839	10.500	50.000	51.091

38.	7.050	4.356	9.956	9.375	55.900	56.681
39.	4.300	2.657	6.072	15.000	72.600	74.133
40.	1.100	0.680	1.553	-18.000	50.700	53.800
41.	1.900	1.174	2.683	-7.500	91.700	92.006
42.	13.400	8.279	18.923	N/A	80.700	N/A
43.	7.500	4.634	10.591	3.750	60.600	60.716
44.	3.150	1.946	4.448	40.000	64.200	75.642
45.	0.200	0.124	0.282	40.000	96.900	104.831
46.	1.500	0.927	2.118	3.000	58.300	58.377
47.	12.650	7.816	17.864	N/A	91.800	N/A
48.	9.650	5.962	13.628	1.875	59.700	59.729
49.	5.900	3.645	8.332	7.500	98.100	98.386
50.	2.100	1.297	2.966	42.000	86.300	95.978
51.	1.200	0.741	1.695	1.500	97.600	97.612
	South Bar					
52.	14.200	9.073	20.739	N/A	47.100	N/A
53.	9.450	6.674	15.254	N/A	122.500	N/A
54.	1.150	2.481	5.671	-1.875	65.700	65.727
55.	3.450	-0.157	-0.359	3.750	83.100	83.185
56.	6.200	1.232	2.816	N/A	64.500	N/A
57.	15.100	8.878	23.674	N/A	50.000	N/A
58.	7.050	4.811	12.830	0.000	52.300	52.300
59.	0.700	1.604	4.276	0.000	47.200	47.200
60.	2.950	0.240	0.641	3.750	54.900	55.028
61.	5.300	1.427	3.806	N/A	56.900	N/A
62.	10.250	5.528	18.236	N/A	63.800	N/A
63.	4.600	2.674	8.820	0.000	56.300	56.300
64.	0.450	0.577	1.905	-1.875	47.400	47.437
65.	2.700	1.014	3.345	N/A	72.100	N/A
66.	5.650	2.504	8.261	N/A	57.200	N/A
	North Lobe					
67.	3.300	2.586	7.882	11.250	8.500	14.100
68.	1.000	0.993	3.026	26.250	28.600	38.820
69.	2.000	1.086	3.309	22.500	30.400	37.821
70.	5.350	3.407	10.383	16.250	10.300	19.239
71.	6.950	4.515	13.761	N/A	20.400	N/A
72.	2.850	1.975	6.018	17.500	21.700	27.877
73.	0.950	0.658	2.006	24.375	31.800	40.067
74.	2.350	1.628	4.962	20.625	28.600	35.261
75.	6.800	4.711	14.359	N/A	43.400	N/A
76.	8.700	6.028	18.371	N/A	61.000	N/A